

Engineered entropic forces allow ultrastrong dynamical backaction

Andreas Sawadsky, Raymond A. Harrison, Glen I. Harris, Walter W.

Wasserman, Yasmine L. Sfendla, Warwick P. Bowen,* and Christopher G. Baker

ARC Centre of Excellence for Engineered Quantum Systems,

School of Mathematics and Physics, University of Queensland, St Lucia, QLD 4072, Australia.

(Dated: August 12, 2022)

When confined within an optical cavity, light can exert strong radiation pressure forces. Combined with dynamical backaction, this enables important processes such as laser cooling, and applications ranging from precision sensors to quantum memories and interfaces. However, the magnitude of radiation pressure forces is constrained by the energy mismatch between photons and phonons. Here, we overcome this barrier using entropic forces arising from the absorption of light. We show that entropic forces can exceed the radiation pressure force by eight orders of magnitude, and demonstrate this using a superfluid helium third-sound resonator. We develop a framework to engineer the dynamical backaction from entropic forces, applying it to achieve phonon lasing with a threshold three orders of magnitude lower than previous work. Our results present a pathway to exploit entropic forces in quantum devices, and to study nonlinear fluid phenomena such as turbulence and solitons.

Introduction

Light generally interacts only weakly with mechanical objects. However, it has been shown that strong interactions can be achieved by confining the light in an optical cavity and employing a low-dissipation mechanical resonance [1]. These cavity optomechanical devices have enabled new physics such as laser amplification and cooling of mechanical motion [2], and new technologies such as precision sensors [3–6]. Remarkably, it has even been possible to reach quantum regimes, where the interaction can create non-classical states of light and of mechanical motion [7, 8] and can enable quantum memories and interfaces, among other quantum technologies [9, 10].

Usually, the optical forces are achieved using radiation pressure or electrostriction [1, 2]. In these cases, it is generally considered desirable to operate in the *resolved sideband regime*, for which the cavity lifetime is longer than the period of the mechanical resonance [10, 11]. However, this prevents multiple scattering processes so that each incident photon can only add or subtract a maximum of one phonon [11]. This introduces a fundamental barrier to the strength of forces that can be imparted by light—the maximum efficiency with which energy may be converted from light into mechanical motion is given by the ratio of mechanical to optical frequencies. This ratio is typically in the range of 10^{-9} to 10^{-5} . Multiple scattering is possible in the reverse, *non-resolved sideband regime* [10, 11]. However, in this regime the interaction is suppressed due to the mismatch between the timescales of cavity decay and mechanical motion [12].

Optical forces can alternatively be applied via entropy gradients, instead of energy gradients. Entropic forces are common in nature, for example, explaining many molecular forces [13, 14] and the restoring force of a stretched rubber band [15]. Entropic optical forces arise due to absorption of photons, and the resulting heat

transfer. Generally known as *photothermal forces*, they can allow dynamical backaction effects such as laser cooling of mechanical motion [16], including into the quantum regime [17, 18]. Interestingly, they can evade the compromise between the number and timescale of interactions that is present for radiation pressure. Operating in the non-resolved sideband regime allows multi-phonon scattering, while the timescale of the interaction can be controlled via the delay introduced during heat transfer [16, 19–21]. This promises orders of magnitude stronger optical forces, but has yet to be achieved. This is, in part, due to the complexities of calculating the strength of the interaction and designing devices to leverage it [21].

Here we demonstrate entropic forces in an optomechanical device that are eight orders-of-magnitude stronger than would be possible with radiation pressure alone. We use them to demonstrate optomechanical phonon lasing with a threshold power of only a few picowatts, a factor of 2000 lower than has been shown before [22]. This phonon laser can be viewed as a microscale thermodynamic heat engine. We show that its efficiency—while low due to the small temperature differential introduced by photon absorption—is nonetheless around a hundred times higher than previous nanomechanical heat engines [23, 24], and could be increased above 10% in purpose-designed devices. Crucial to enabling these results, we develop a new broadly applicable methodology to model optomechanical entropic forces and the dynamical backaction they cause.

Our optomechanical device exploits third sound resonances of a superfluid helium thin film as the mechanical element [25–28]. This choice of mechanical element allows the precise engineering of entropic forces, leveraging both entropy-driven fountain pressure, which exists only in superfluids, and the ability to tune the thermal properties of the system over many orders of magnitude via small changes in temperature, film-thickness, and geometry. Combined with the much higher com-

* w.bowen@uq.edu.au

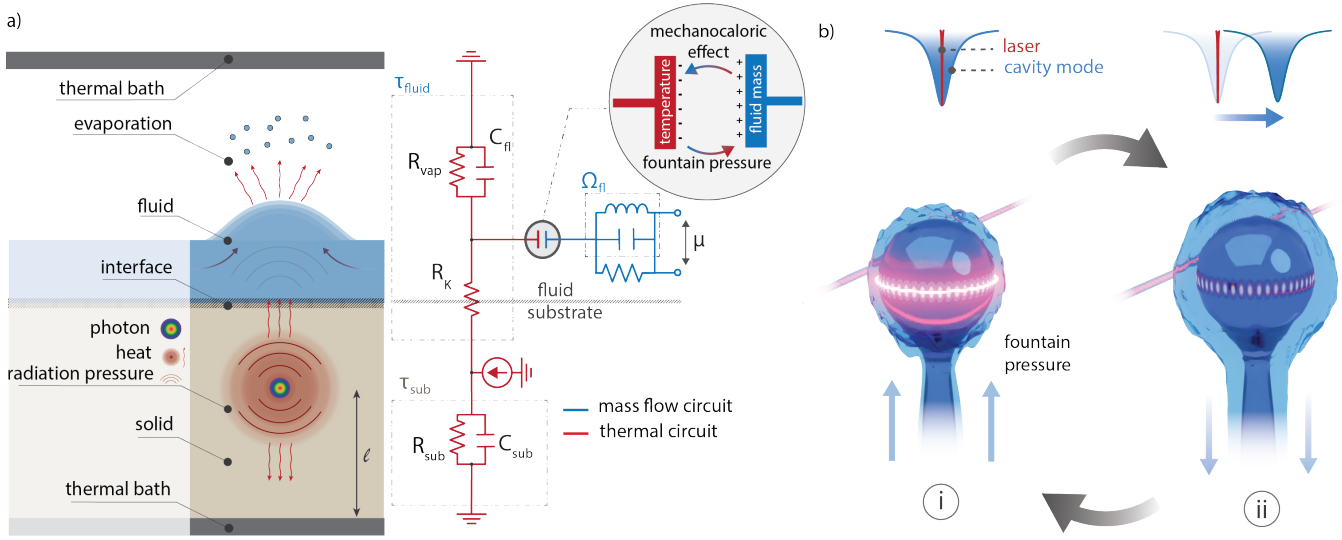


FIG. 1. (a) Left: Cross-section schematic showing the superfluid and heat flow in response to photon absorption. Right: Thermal equivalent circuit (red) coupled to the superfluid mass flow circuit (blue). R : thermal resistance; C : heat capacity; μ : chemical potential; 'K', 'sub', 'vap', 'fl' refer respectively to Kapitza, substrate, vapor and fluid (see Supplementary Material B). (b) Superfluid optomechanical resonator used in the experiments: fiber-coupled silica microsphere on a silica stem, covered by a ~ 24 nm superfluid film (blue). Illustration of the optomechanical feedback loop between superfluid motion and intracavity power responsible for dynamical backaction [11].

pliance of liquids compared to solids [29–31], this offers the potential for a broad range of applications, beyond those enabled by dynamic backaction. For instance, the generation of quantized vortices and solitons, as well as all-optical wavelength tuning of microcavities and single photon counting.

Results

Modelling and optimising entropic forces

Photon absorption events cause a local change in the superfluid temperature, which introduces a fountain (entropic) pressure between hot and cold regions. This drives superfluid flow towards the heat source [32–34] (the thermomechanical effect [35]), and in bulk superfluid helium drives normal fluid counterflow. These flows exert forces on the superfluid that can be used to drive superfluid sound modes [27]. Similar to other thermomechanical forces [16], the forces are not instantaneous. Rather, they react over the thermal response time τ , which depends on both the properties of the superfluid and the vessel in which it resides. The time delay introduces dynamical backaction that can be used to both cool and amplify the motion of the superfluid [27, 29]. Optimisation of this entropic backaction requires both that the fountain pressure is maximized and that

the condition $\Omega\tau \sim 1$ is met, where Ω is the resonance frequency of the superfluid mode. This condition corresponds to the optimal delay in the optical force for efficient energy transfer [17, 20]. The fountain pressure is given by $\Delta p = \rho S \Delta T$, where ρ , ΔT , and S are respectively the superfluid density, local temperature change, and entropy [33]. Employing this relation and extending known results for other thermomechanical forces [17–19],

we find that the effective dynamical backaction force is given by $F = \rho S \Delta T \mathcal{A} \times \left(\frac{\Omega\tau}{1 + \Omega^2\tau^2} \right)$, where \mathcal{A} is the effective area of the sound mode, including any spatial mismatch between the mode and the fountain pressure force.

To model the entropic forces and entropic backaction, we consider the general system geometry shown in Fig. 1(a). This consists of a superfluid reservoir in contact with a solid substrate and a vapor-phase environment. These, in turn, are in contact with a thermal bath at temperature T . Light interacts with the system via photon absorption events which, due to the vanishingly small optical absorption of superfluid helium [36], are assumed to occur only within the substrate. Heat from absorption events can dissipate either directly into the thermal bath, or by propagating into the superfluid through the interfacial Kapitza resistance and then via evaporation of helium into the vapor-phase.

The Kapitza conductance (R_K^{-1}) scales with the cube of temperature, while the effective thermal conductance of evaporation (R_{vap}^{-1}) increases exponentially with temperature (see Supplementary Material B). Small temperature changes can also change the superfluid entropy and thermal conductivity of the substrate by orders of magnitude, while the geometry of the superfluid-coated device can greatly affect the temperature change ΔT induced by optical absorption, the frequency of the sound mode, and the thermal anchoring of the superfluid. As we will see in the following, these strong dependencies provide a powerful means to either leverage strong fountain pressure forces at low temperatures, or suppress them at high temperatures so that the unitary radiation pressure in-

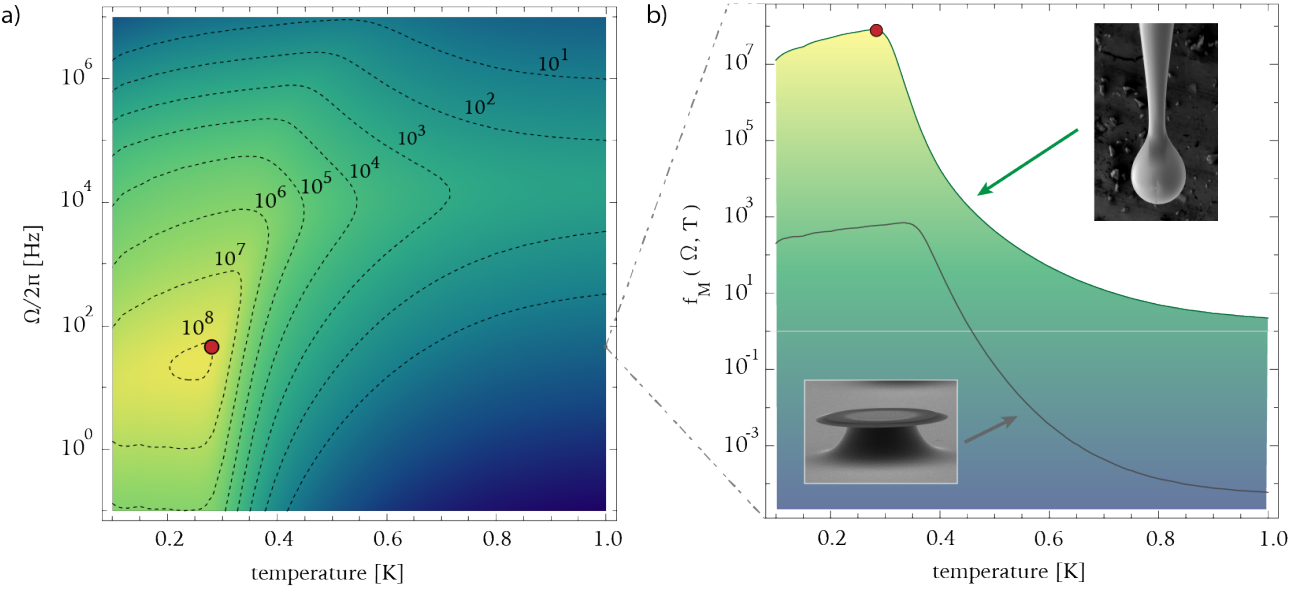


FIG. 2. (a) Contour plot of the figure of merit $f_M(\Omega, T)$, indicating the optimal operating point for enhanced photothermal backaction, as a function of cryostat temperature T and third sound frequency $\Omega/2\pi$. (b) Cut through the dashed white line in (a), showing the figure of merit $f_M(2\pi \times 72, T)$ for our microsphere resonator (solid line). The grey line plots the same figure of merit for our previous silica microdisk experimental geometry [29] (calculated with $\Omega = 2\pi \times 7$ MHz), for which the optomechanical forces should be entirely dominated by radiation pressure at temperatures above 500 mK. The horizontal line marks the boundary between the fountain pressure and the radiation pressure-dominated regimes (situated above and below respectively). Red dot in (a) and (b) marks our experimental operating point.

teraction can be exploited.

To enable quantitative predictions, we develop an electric circuit analogue model (right panel, Fig. 1(a)). This model combines a thermal circuit (red) that represents heat flow, a fluid-flow circuit (blue) that represents superfluid mass flow, and a lumped-element RLC circuit that represents the superfluid sound mode. The thermal and fluid-flow circuits are connected via an effective capacitor which accounts for the fact that a temperature difference drives a superflow via the fountain pressure, while conversely a superflow affects the temperature via the *mechanocaloric* effect [37]. The current, voltage, resistance and capacitance in the electric circuit are respectively the analogs of heat flow \dot{Q} , temperature T , thermal resistance and heat capacity, while a chemical potential difference μ drives a mass flow \dot{m} in the superfluid. For a given geometry and temperature, we determine the parameters of the circuit using a combination of existing data and finite-element modelling. We are then able to simulate the dynamics of the sound mode, including entropic forcing and entropic backaction. The simulation ultimately yields a complex transfer function, providing both the amplitude and phase response of the superfluid sound mode (see Supplementary Material Section B).

As a specific application of our analogue electric circuit model we consider a few nanometer-thick superfluid film self-assembled on a microsphere (Fig. 1(b)). Due to the thinness of the film only the superfluid component can move, as the normal fluid component is vis-

ously clamped [34]. The superfluid component sustains third sound waves, similar to shallow water waves, due to the van der Waals restoring force between the superfluid and the microsphere surface [27, 28, 38–40]. The microsphere is suspended on a stem which is attached to a flat substrate. The substrate creates an effective boundary, confining resonant third sound modes. These ‘stem modes’ present as oscillations in the film thickness that flow back and forth along the stem, as illustrated in Fig. 1b (i) and (ii). Their resonance frequencies Ω can be conveniently tuned by changing the length l of the stem, or by tuning the film thickness and therefore the strength of the van der Waals force. Their motion can be optically driven and observed by exploiting optical whispering gallery mode (WGM) resonances that exist within the microsphere [27].

We choose to study the fundamental stem mode, which features a single antinode at the microsphere and a single node at the substrate. Since the antinode coincides with the position of the optical whispering gallery mode, its motion is well coupled to the WGM resonance. Modelling shows that in our regime the thermal conductivity is such that optical absorption events act to raise the temperature of the entire microsphere-stem system, so that the effective area \mathcal{A} over which the force is applied is, to good approximation, equal to the total surface area of the system. Using these assumptions, we calculate all parameters of the analogue circuit model in Supplementary Material B. This allows us to predict the effective

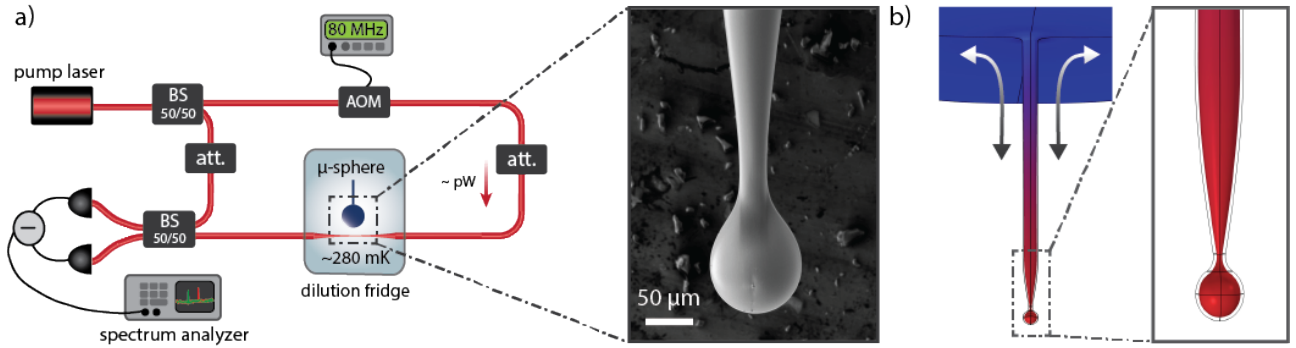


FIG. 3. (a) Simplified heterodyne experimental setup schematic, including beam splitters (BS), attenuator (att.) and acousto-optic modulator (AOM). Inset shows a scanning electron microscope (SEM) image of the microsphere. (b) Finite element simulation showing the fundamental superfluid third sound mode confined to the surface of the microsphere resonator (incl. stem), obtained by solving the Helmholtz equation on the resonator's outer surface (see Supplementary Material A 3). Inset shows the displacement profile at the level of the spherical tip, where the WGM field is located.

entropic dynamical backaction force F .

Our model predicts that there exists an optimal combination of temperature and mechanical resonance frequency to maximise the dynamical backaction force. We find that the optimal resonance frequency coincides with the resonance frequency of the fundamental stem mode if a stem length of $l \sim 2$ mm is chosen, and that for this stem length the optimal temperature of $T \simeq 250$ mK is easily experimentally accessible. To remove any dependence on laser power, we normalize the dynamical backaction force F by the radiation pressure force $F_{\text{rad}} = n_{\text{cav}} \hbar G$ [11], where n_{cav} is the number of photons within the resonator and $G/2\pi = 0.2$ GHz/nm the radiation pressure optomechanical coupling rate (see Supplementary Material section A 4). This provides the dimensionless figure of merit $f_M = F/F_{\text{rad}}$ shown in Fig. 2(a) as a function of both temperature and mechanical resonance frequency, for a microsphere WGM resonator that we fabricated which has a stem length of $l = 1.8$ mm. As can be seen, f_M is predicted to be sharply peaked, varying by more than seven orders of magnitude as the temperature is changed by a factor of ten, and also varying strongly with resonance frequency. At its optimum, the fountain pressure force is predicted to be over 8 orders of magnitude larger than the radiation pressure force.

To further illustrate the significant gains that can be achieved through optimisation, we calculate the same figure of merit for the microdisk superfluid optomechanical system reported in Ref. [29]. In that work, phonon-lasing occurred on a high-order Brillouin sound mode at $\Omega/2\pi = 7$ MHz. This is shown in Fig. 2(b) as a function of temperature, alongside the microsphere for comparison. While the trends are similar, the peak value is close to 5 orders of magnitude lower for the microdisk. Our modelling moreover shows that for temperatures in excess of 500 mK, the superfluid becomes much more strongly thermally anchored to the cryostat through its vapor phase than to the substrate. This effectively thermally decouples the superfluid from the microresonator,

switching off the fountain pressure interaction. Temperature control therefore provides a useful lever (unexploited in previous work) to either leverage strong fountain pressure forces at low temperatures, or focus on the unitary radiation pressure interaction at higher temperatures.

Experimental validation

To validate the predictions of our model, we locate our microsphere WGM device within a superfluid-tight enclosure whose temperature can be precisely tuned between $T = 10$ mK and $T = 1.5$ K. A narrow capillary enables the film thickness to be changed in-situ, ranging from a few atomic monolayers to a maximum reached at the saturated vapor pressure, where the sphere is uniformly coated with a $d \simeq 24$ nm thick superfluid film (~80 atomic layers), see Supplementary Material A 2. By controlling the bath temperature T and the stem-mode frequency (through superfluid film thickness) we are able to operate at the near-optimal experimental setting where the fountain pressure is maximized and the mechanical frequency matches the thermal response, with $\Omega\tau = 0.94$, marked by the red dot in Fig. 2(a) and Fig. 2(b).

We optically excite the WGM resonator via evanescent coupling of 1554 nm light from a tapered optical fiber placed in its close proximity, achieving critical coupling to a WGM with intrinsic dissipation rate $\kappa_i/2\pi = 15$ MHz. The time-delayed fountain pressure forcing this modifies the dynamics of the fundamental stem mode through the introduction of an effective optomechanical damping rate Γ_{ent} . The sign of this modification may be positive, leading to cooling of the sound mode [27], or negative, leading to amplification [29]. In the latter case, phonon lasing occurs once the magnitude of optomechanical (anti-) damping exceeds the intrinsic acoustic damping rate Γ [10, 16, 17, 20]. A measure of the strength of the light-superfluid interaction is provided by the power and intracavity photon number at which this regime is reached.

We employ the heterodyne readout scheme shown in Fig. 3(a) to measure the power spectra of superfluid os-

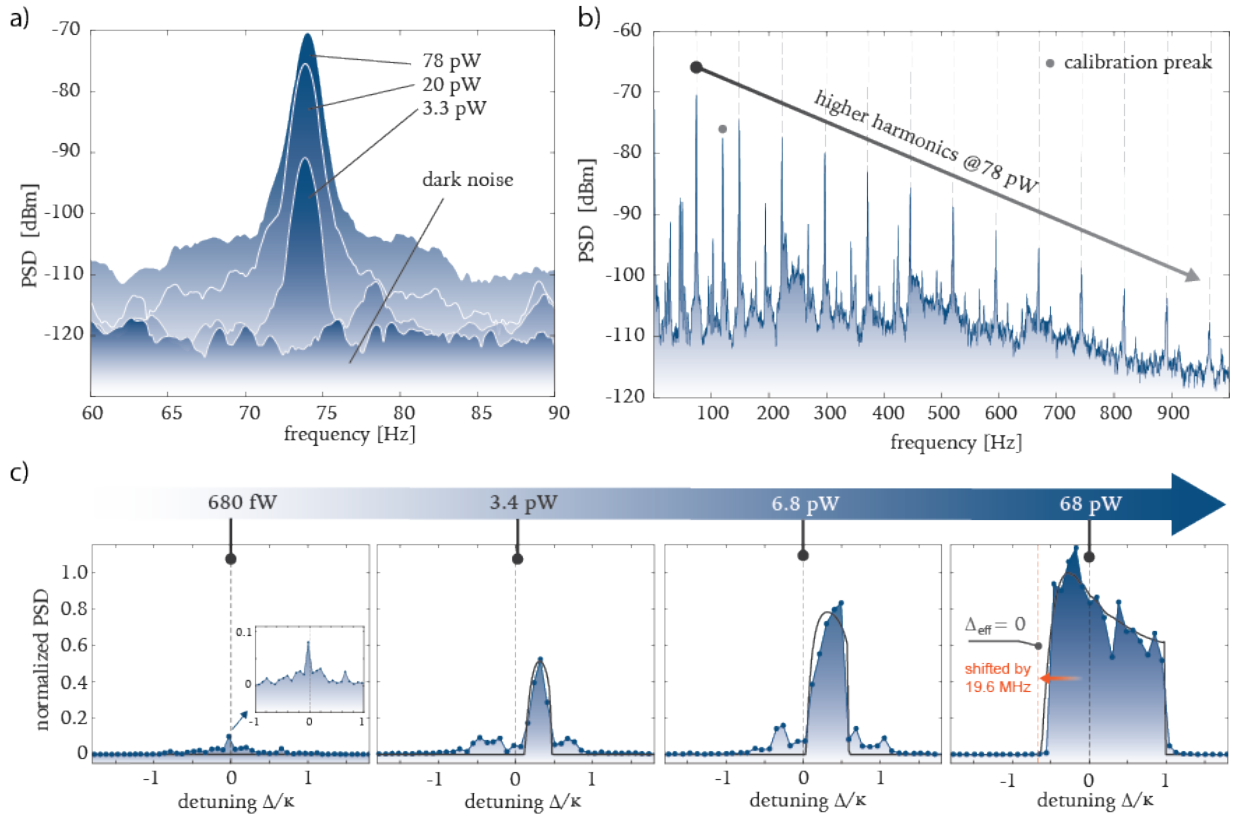


FIG. 4. Entropic backaction driven phonon lasing. a) Power spectral density (PSD) of the fundamental stem mode at $\Omega_M/2\pi = 72$ Hz lasing at different input powers. (b) Broader power spectrum at an input power of 78 pW showing 12 higher harmonics of the fundamental mode Ω_M . The peak marked by the gray dot is an introduced calibration peak. c) Lasing threshold measurement and the corresponding ODE simulations. Each sub-figure corresponds to different input power, which is increasing from 680 fW to 68 pW. Each blue point corresponds to the peak power spectral density at Ω_M for a laser detuning Δ with respect to the cavity resonance, while the black line shows the results of the ODE simulation. At 68 pW the lasing appears to occur for both positive and negative cavity detunings. This is due to steady-state optical heating of the WGM resonator by around 3.6 mK above $T = 284$ mK (see Supplementary Material Fig. 15). This DC heating causes an influx of superfluid shifting the resonance frequency by 19.6 MHz, in good agreement with simulations, and corresponds to a tunability of 288 GHz/ μ W.

cillation for various input powers. These are shown in Fig. 4(a). The sharp peak observed at the expected frequency of the fundamental stem mode is characteristic of phonon-lasing for cryostat temperatures over the range from 100 mK to 500 mK. We find that the phonon-lasing peak appears for the lowest laser powers at a temperature of around 280 mK, consistent with the predictions of our model. At this temperature the peak is visible even for powers as low as a few picowatts, while for the higher power of 78 pW more than 10 higher harmonics are seen (see Fig. 4(b)). These harmonics indicate that the phonon lasing has reached motional amplitudes that are sufficiently large to detune the optical cavity significantly away from resonance with the excitation field, thereby introducing a transduction nonlinearity.

To confirm that the observed behavior is phonon lasing and to constrain the threshold optical drive power, we sweep the laser wavelength over the cavity resonance (from blue- to red-detuned) for various input powers. A

characteristic feature of dynamical backaction is that the sign of the optomechanical damping it introduces is opposite on either side of the resonance. We therefore expect to observe lasing on one side of resonance and cooling on the other. For each power and detuning we measure the power spectrum to determine the peak of the dynamic response of the stem mode. In Fig. 4(c) we plot the normalized peak power spectral density versus detuning for input powers of 680 fW, 3.4 pW, 6.8 pW and 68 pW. At the lowest input power of 680 fW the measured mode amplitude (blue dots) is low and symmetric around the cavity resonance. This indicates limited dynamical back action. At an input power of 3.4 pW the measured mode amplitude is about four times higher on the heating side (blue-detuned) compare to the cooling side (red-detuned), indicating that phonon lasing is occurring. At this point, the superfluid oscillator is in a regime of large coherent oscillations with amplitude ~ 1 Å, modulating the intensity of the transmitted optical

field by more than 60%. This provides further confirmation that phonon-lasing is occurring, since, in the absence of other nonlinearities, a large modulation is required to suppress the exponential growth in phonon lasing to a constant amplitude in the steady state. The modulation does this by reducing the average intracavity power, and therefore the steady-state gain of the phonon lasing process [41]. At higher powers again, both the asymmetry and lasing amplitude increase further. These results are in good agreement with numerical simulations (black line) solving the coupled equations of motion for the intracavity field, superfluid motional amplitude and temperature (see Supplementary Material Section C for more details). Our results indicate that the phonon lasing threshold is in the range of 1 to 3.4 pW, corresponding to an average of less than 0.2 intracavity photons. This threshold is more than three orders of magnitude lower than previous reported values for optically driven optomechanical resonators [22].

Figure 5 compares the phonon-lasing threshold achieved in our work to the state-of-the-art as a function of the effective mass of the mechanical resonator. Prior experiments have used radiation pressure (orange dots), electrostrictive (orange dots), electrothermal (green dots) and photothermal (blue dots) forces. Most of them form a cluster with microwatt-range threshold powers and picogram-range effective masses. Only electrothermally-driven carbon nanotube resonators reach thresholds approaching a picowatt [23, 24]. A significant attribute that enables this is their attogram-level effective mass. This exceptionally low mass allows large motional amplitudes to be driven with small forces. By exploiting engineered entropic backaction, our results operate in a vastly different parameter space, breaking the trend between threshold power and effective mass. Indeed, our 5 gram effective mass is 18 orders of magnitude larger than electrothermally driven systems and 8 orders of magnitude larger than other, much higher threshold, systems.

Thermodynamic efficiency

The larger mass of our system compared to other extremely low threshold phonon lasers is partly offset by the superfluid resonator's lower frequency, since the stored mechanical energy scales as $m_{\text{eff}}\Omega^2$. A more complete picture emerges when comparing the systems' thermodynamic efficiencies, which account for the overall optical to acoustical energy conversion.

Our optomechanical phonon laser can be thought of as a heat engine converting heat into mechanical work, with the superfluid film acting as the working medium, the cryostat acting as the cold reservoir and the heated region of the microsphere acting as the hot reservoir. We can estimate its thermodynamic efficiency η by comparing the mechanical power P_{mech} supplied to the superfluid oscillator to sustain its oscillations to the optical power dissipated in the resonator P_{abs} . At an input power of $P = 6.8 \text{ pW}$, well above the onset of lasing, this yields $\eta = \frac{P_{\text{mech}}}{P_{\text{abs}}} = \frac{1}{2}m_{\text{eff}}\Omega^2x^2\Gamma/(P \times \alpha_{\text{abs}}) \simeq 10^{-5}$ (see Supplementary Material, Section E).

This can be compared to the Carnot limit $\eta_{\text{max}} = 1 - \frac{T_C}{T_H}$ determined by the temperature of the hot and cold reservoirs T_H and T_C . Here $T_C = T$ is the cryostat temperature, and $T_H = T + \Delta T$ the temperature of the heated microresonator. At $P = 6.8 \text{ pW}$, our numerical simulations show that $T_C = 284.0 \text{ mK}$ and $T_H = 284.4 \text{ mK}$ (see Supplementary Material Section C & Fig. 14), such that $\eta_{\text{max}} \simeq 10^{-3}$. This means the system operates within two orders of magnitude of the thermodynamic limit. One reason that it does not reach this limit is that the hot and cold reservoirs are thermally linked through the stem, leading to significant thermal losses.

While the efficiency we achieve is low, to our knowledge it is nonetheless the highest optical-to-mechanical conversion efficiency reported in an optomechanical device. Indeed, the nonlinear radiation pressure scattering interaction between a photon of frequency ω and a mechanical oscillator of frequency Ω leads to an energy transfer $\hbar\Omega$ in the resolved sideband regime (where $\Omega > \kappa$ [10, 11]), providing an upper bound of $\eta \leq \Omega/\omega$. Gigahertz frequency optomechanical crystals [22] operate in a regime where this fraction reaches up to $\Omega/\omega \sim 2.5 \times 10^{-5}$, however the total efficiency is suppressed by a factor of $Gx/\omega \ll 1$ due to the low rate at which photons enter the cavity via the upper motional sideband [11]. Alternatively, when operating in the unresolved sideband regime ($\kappa \gg \Omega$), each photon can generate many phonons—corresponding to the generation of a large number of higher order motional sidebands. This has been employed to excite mechanical oscillators to very large amplitudes, corresponding to occupations upwards of 10^{12} phonons [12], but the efficiency was limited by the lower phonon energy.

In both of the above cases, as well as for low threshold microtoroid resonators [1], efficiencies are in the 10^{-8} to 10^{-7} range.

Our efficiency is additionally significantly larger than that of photothermally-driven resonators reported in the literature [16, 20], where η was on the order of 10^{-12} . It is also two orders of magnitude higher than

the efficiency of 10^{-7} achieved for an electrothermally-driven carbon nanotube in Ref. [24], which has the lowest previously reported phonon-lasing threshold (data point 1 in Fig. 5, and Supplementary Material Section E).

The higher efficiency reported here can be understood by considering that our optomechanical device operates in the unresolved sideband regime, enabling efficient on-resonance pumping of the cavity, while simultaneously operating in the resolved sideband regime as far as the time delay is concerned. Indeed, in radiation pressure driven systems, the optimal time-delayed forcing criterion $\Omega\tau_{\text{rp}} \sim 1$ is equivalent to $\Omega \sim \kappa$ (resolved sideband regime), which consequently requires inefficient off-resonant driving of the cavity. Here, since the delay is no longer provided by the finite lifetime of the photons in the cavity $\tau_{\text{rp}} = 1/\kappa$, but by an independently controllable thermal response time τ , this tension is relieved, enabling a combination of on resonance driving and ef-

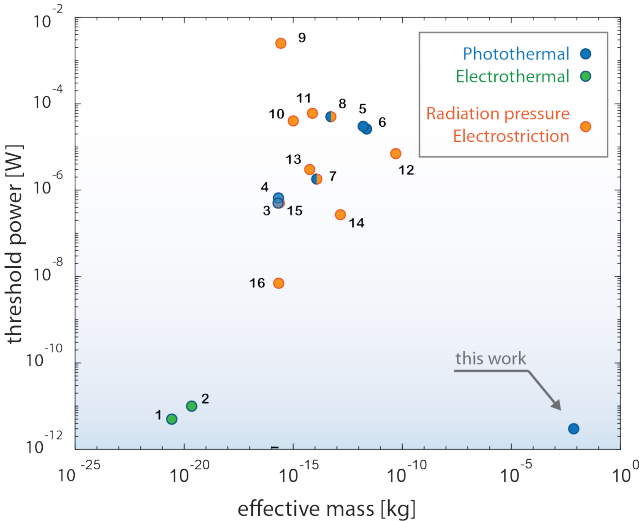


FIG. 5. Phonon lasing thresholds of different optomechanical and electromechanical published experiments plotted versus the effective mass of the mechanical mode. The reference publication for each point can be found in Supplementary Material D.

ficient dynamical backaction $\Omega\tau \sim 1$. This allows us to employ a broad optical resonance enabling a greater dynamic range [41] and larger mechanical amplitudes to be reached, while maintaining a large time delay τ for the optical forcing (equivalent to what would be achieved by an optical cavity with Q of 2×10^{12}).

The thermodynamic efficiency could be further improved by reducing the volume of the resonator. Indeed, the microsphere volume, including the stem, is on the order of $10^6 \mu\text{m}^3$. This can be reduced by approximately six orders of magnitude to $\sim 1 \mu\text{m}^2$ through the use of smaller mode volume resonators such as photonic crystal resonators [42] or high index WGM cavities [43]. The reduced thermal mass then leads to a smaller ratio of T_C/T_H , and predicted efficiencies $\eta_{\max} > 10\%$, commensurate with the highest reported values for the efficiency of superfluid fountain-effect pumps [44].

Discussion

As discussed earlier, at the operating point of our experiments the entropic forces are around 10^8 stronger than the radiation pressure forces. Moreover, the dimensionless term $\left(\frac{\Omega\tau_{\text{fp}}}{1+\Omega^2\tau_{\text{fp}}^2}\right)$, where $\tau_{\text{fp}} = 1/\kappa$ is the photon decay rate, which quantifies the efficiency of the time-delayed radiation-pressure forcing for dynamical backaction [10, 16–19] is only 2×10^{-6} for the acoustic mode considered here. In contrast the equivalent term for fountain pressure is of order $1/2$. Combined, this means that the optimized fountain pressure dynamical backaction is over 13 orders of magnitude more effective, enabling the efficient driving of low frequency superfluid acoustic modes in a regime where the radiation pressure fails. We expect this to have important consequences for the study of superfluid nonlinear hydrodynamical phenomena such

as solitonic behaviour [45] and vortex stirring [28], where the ability to drive and monitor large amplitude wave motion without boiling the film is critical.

It is natural to ask whether the strong forcing achieved here is due to a unique property of the fountain pressure force. We note however that the fountain pressure per absorbed photon is of similar magnitude to the thermoelectric stress which would occur in a crystalline material (see Supplementary Material G). It is thus primarily the engineered ability to collect the thermal energy and operate near the optimal regime $\Omega\tau \sim 1$, combined with the compliance of the fluid interface which is responsible for the ultralow threshold observed here, and not a fundamentally stronger nature of the fountain pressure force in superfluid helium, making these results broadly applicable to photothermally- and electrothermally-driven systems. The model presented here can also be applied to a variety of different fluids, with some straightforward modifications.

Compared to solids, fluids provide a pathway towards strongly enhanced light-matter interactions, thanks to their compliant interfaces. Early work by Ashkin et al. used radiation pressure from a focussed laser beam to deform an air-liquid interface, using the direction of the deflection (outward) to answer open questions about the momentum of photons in a dielectric [46]. The malleability of liquid-liquid and liquid-air interfaces has also been leveraged in optofluidic devices such as adaptive lenses and ‘lab-on-chip’ applications [47], as well as for fluidic optomechanical resonators [48], the generation of giant optical nonlinearities [49], and transformable optical cavities [30]—which have been proposed to reach the single-photon nonlinear regime [31]. With the thick ($d = 24 \text{ nm}$) film considered here, the van der Waals pressure $P_{\text{vdW}} = \frac{\rho\alpha_{\text{vdW}}}{d^3}$, which opposes surface deformation and plays the role of the Young’s modulus in a solid, is two billion times softer than the underlying silica sphere [40]. The consequence of this compliance extends here beyond dynamical backaction into large static deformations and optical tunability. Indeed, steady-state optical heating of the WGM resonator causes a DC fountain pressure which locally thickens the film. This changes the effective radius of the cavity, shifting the resonance frequency. At an input power of 68 pW , a DC heating of around 3.6 mK above the bath temperature of $T = 284 \text{ mK}$ (see Fig. 15 in the Supplementary Material) shifts the resonance by 19.6 MHz , as shown in Fig. 4 c). This shift corresponds to an exceptionally high all-optical tunability of $288 \text{ GHz}/\mu\text{W}$, nearly three orders of magnitude larger than that achieved with purpose-built all optical wavelength routing systems based on mechanically compliant nano-optomechanical resonators [50]. It is also well in excess of the highest reported values for thermal tuning of microresonators ($0.26 \text{ GHz}/\mu\text{W}$) [51]—albeit with the constraints of cryogenic operation and reduced response rate—underscoring the strength of this optomechanical interaction. In the scenario where the volume of the resonator is reduced to the order of $\sim 1 \mu\text{m}^2$, its ther-

mal mass becomes dominated by the helium film itself, and the achievable fountain pressure per absorbed photon takes the simple, temperature independent expression $P_{\text{fp}} \simeq \frac{\hbar\omega}{3V_{\text{He}}}$. Using this relation, we find that optical frequency shifts larger than κ are achievable for a single absorbed photon, potentially providing a novel approach to single photon detection (see Supplementary Material F).

Finally, this work may lay the groundwork for transformable *phononics*, where optically defined acoustic circuits may be formed on demand. Indeed, DC radiation pressure and/or fountain pressure contributions can substantially thicken the film, as mentioned in the context of optical tuning. This thickening also reduces the speed of sound $c_3 = \sqrt{3\alpha_{\text{vdW}}d^{-3}}$ within the optically defined ‘bulge’. Thus, much like an optical waveguide where light is trapped in a higher refractive (lower speed) medium, this could be used to optically trap sound waves [52]. Optomechanical backaction in this regime would represent a new form of dynamical backaction between the intensity of light within a cavity and the shape of the mechanical eigenmodes that it creates, rather than with the momentum of an independently defined mechanical resonator.

Materials and Methods

Experimental setup

The microsphere resonator is formed by melting the tapered end of a silica single-mode fiber (SMF-28) in a fusion splicer. It is then mounted by its non-reflow end inside a superfluid-tight sample chamber within a dilution refrigerator at a temperature $T = 284$ mK. Infrared laser light ($\lambda = 1554$ nm) from a low-noise erbium-doped fiber

laser is evanescently coupled into the microsphere via a tapered optical fiber [27]. Helium gas is injected via a capillary to form a $d = 24$ nm-thick saturated superfluid ^4He film covering the microsphere resonator [27, 29, 32] (see supplementary material A for more details). The optical WGMs possess an evanescent component which extends outside the resonator, and are therefore sensitive to the refractive index perturbation caused by the presence and motion of the superfluid [40]. This leads to a frequency shift of the WGM resonances $\Delta\omega_0 = G \times d$, where $G/2\pi = 0.2 \pm 0.01$ GHz/nm is the optomechanical coupling rate (see supplementary material A 4). High sensitivity optical readout of the superfluid’s acoustic modes is performed with a heterodyne detection scheme with a local oscillator field offset by 80 MHz [29], as shown in Fig. 3(a). Because of the 9 orders of magnitude difference between probe and local oscillator beam powers (pW vs mW), care must be taken to avoid any back-reflections, even as small as those occurring on the facets of the balanced detector. This is done here with a circulator positioned after the microsphere (not shown in Fig. 3(a)).

Funding

This work was funded by the US Army Research Office through grant number W911NF17-1-0310 and the Australian Research Council Centre of Excellence for Engineered Quantum Systems (EQUS, project number CE170100009). C.G.B and G.I.H respectively acknowledge Australian Research Council Fellowships DE190100318 and DE210100848.

Disclosures

The authors declare no conflicts of interest.

- [1] T. Kippenberg, H. Rokhsari, T. Carmon, A. Scherer, and K. Vahala, “Analysis of radiation-pressure induced mechanical oscillation of an optical microcavity,” *Physical Review Letters*, vol. 95, no. 3, p. 033901, 2005.
- [2] J. Chan, T. P. M. Alegre, A. H. Safavi-Naeini, J. T. Hill, A. Krause, S. Gröblacher, M. Aspelmeyer, and O. Painter, “Laser cooling of a nanomechanical oscillator into its quantum ground state,” *Nature*, vol. 478, pp. 89–92, Oct. 2011.
- [3] A. G. Krause, M. Winger, T. D. Blasius, Q. Lin, and O. Painter, “A high-resolution microchip optomechanical accelerometer,” *Nature Photonics*, vol. 6, no. 11, pp. 768–772, 2012.
- [4] S. Basiri-Esfahani, A. Armin, S. Forstner, and W. P. Bowen, “Precision ultrasound sensing on a chip,” *Nature Communications*, vol. 10, no. 1, pp. 1–9, 2019.
- [5] T. Purdy, K. Grutter, K. Srinivasan, and J. Taylor, “Quantum correlations from a room-temperature optomechanical cavity,” *Science*, vol. 356, no. 6344, pp. 1265–1268, 2017.
- [6] S. Forstner, E. Sheridan, J. Knittel, C. L. Humphreys, G. A. Brawley, H. Rubinsztein-Dunlop, and W. P. Bowen, “Ultrasensitive optomechanical magnetometry,” *Advanced Materials*, vol. 26, no. 36, pp. 6348–6353, 2014.
- [7] A. H. Safavi-Naeini, S. Gröblacher, J. T. Hill, J. Chan, M. Aspelmeyer, and O. Painter, “Squeezed light from a silicon micromechanical resonator,” *Nature*, vol. 500, no. 7461, pp. 185–189, 2013.
- [8] R. Riedinger, A. Wallucks, I. Marinković, C. Löschnauer, M. Aspelmeyer, S. Hong, and S. Gröblacher, “Remote quantum entanglement between two micromechanical oscillators,” *Nature*, vol. 556, no. 7702, pp. 473–477, 2018.
- [9] R. Delaney, M. Urmey, S. Mittal, B. Brubaker, J. Kindem, P. Burns, C. Regal, and K. Lehnert, “Superconducting-qubit readout via low-backaction electro-optic transduction,” *Nature*, vol. 606, no. 7914, pp. 489–493, 2022.
- [10] W. P. Bowen and G. J. Milburn, *Quantum optomechanics*. CRC Press, 2015.
- [11] M. Aspelmeyer, T. J. Kippenberg, and F. Marquardt, “Cavity optomechanics,” *Reviews of Modern Physics*, vol. 86, pp. 1391–1452, Dec. 2014.
- [12] M. Bagheri, M. Poot, M. Li, W. P. H. Pernice, and H. X. Tang, “Dynamic manipulation of nanomechanical resonators in the high-amplitude regime and non-volatile mechanical memory operation,” *Nature Nanotechnology*, vol. 6, pp. 726–732, Oct. 2011.

[13] S. Asakura and F. Oosawa, "On interaction between two bodies immersed in a solution of macromolecules," *The Journal of Chemical Physics*, vol. 22, no. 7, pp. 1255–1256, 1954.

[14] X. Liu, M. M. Skanata, and D. Stein, "Entropic cages for trapping dna near a nanopore," *Nature Communications*, vol. 6, no. 1, p. 6222, 2015.

[15] L. G. Treloar, *The physics of rubber elasticity*. Oxford University Press, 1975.

[16] C. H. Metzger and K. Karrai, "Cavity cooling of a microlever," *Nature*, vol. 432, no. 7020, pp. 1002–1005, 2004.

[17] J. Restrepo, J. Gabelli, C. Ciuti, and I. Favero, "Classical and quantum theory of photothermal cavity cooling of a mechanical oscillator," *Comptes Rendus Physique*, vol. 12, pp. 860–870, Dec. 2011.

[18] S. De Liberato, N. Lambert, and F. Nori, "Quantum noise in photothermal cooling," *Physical Review A*, vol. 83, p. 033809, Mar. 2011.

[19] C. Metzger, I. Favero, A. Ortlib, and K. Karrai, "Optical self cooling of a deformable Fabry-Perot cavity in the classical limit," *Physical Review B*, vol. 78, p. 035309, July 2008.

[20] C. Metzger, M. Ludwig, C. Neuenhahn, A. Ortlib, I. Favero, K. Karrai, and F. Marquardt, "Self-Induced Oscillations in an Optomechanical System Driven by Bolometric Backaction," *Physical Review Letters*, vol. 101, p. 133903, Sept. 2008. Publisher: American Physical Society.

[21] A. G. Primo, C. M. Kersul, R. Benevides, N. C. Carvalho, M. Ménard, N. C. Frateschi, P.-L. de Assis, G. S. Wiederhecker, and T. P. Mayer Alegre, "Accurate modeling and characterization of photothermal forces in optomechanics," *APL Photonics*, vol. 6, p. 086101, Aug. 2021.

[22] S. M. Meenehan, J. D. Cohen, S. Gröblacher, J. T. Hill, A. H. Safavi-Naeini, M. Aspelmeyer, and O. Painter, "Silicon optomechanical crystal resonator at millikelvin temperatures," *Physical Review A*, vol. 90, p. 011803, July 2014.

[23] Y. Wen, N. Ares, F. J. Schupp, T. Pei, G. a. D. Briggs, and E. A. Laird, "A coherent nanomechanical oscillator driven by single-electron tunnelling," *Nature Physics*, vol. 16, pp. 75–82, Jan. 2020.

[24] C. Urgell, W. Yang, S. L. De Bonis, C. Samanta, M. J. Esplandiu, Q. Dong, Y. Jin, and A. Bachtold, "Cooling and self-oscillation in a nanotube electromechanical resonator," *Nature Physics*, vol. 16, pp. 32–37, Jan. 2020.

[25] K. R. Atkins, "Third and Fourth Sound in Liquid Helium II," *Physical Review*, vol. 113, pp. 962–965, Feb. 1959.

[26] F. M. Ellis and L. Li, "Quantum swirling of superfluid helium films," *Physical review letters*, vol. 71, no. 10, p. 1577, 1993.

[27] G. I. Harris, D. L. McAuslan, E. Sheridan, Y. Sachkou, C. Baker, and W. P. Bowen, "Laser cooling and control of excitations in superfluid helium," *Nature Physics*, vol. 12, pp. 788–793, Aug. 2016.

[28] Y. P. Sachkou, C. G. Baker, G. I. Harris, O. R. Stockdale, S. Forstner, M. T. Reeves, X. He, D. L. McAuslan, A. S. Bradley, M. J. Davis, and W. P. Bowen, "Coherent vortex dynamics in a strongly interacting superfluid on a silicon chip," *Science*, vol. 366, pp. 1480–1485, Dec. 2019.

[29] X. He, G. I. Harris, C. G. Baker, A. Sawadsky, Y. L. Sfendla, Y. P. Sachkou, S. Forstner, and W. P. Bowen, "Strong optical coupling through superfluid Brillouin las-

ing," *Nature Physics*, pp. 1–5, Feb. 2020.

[30] M. Douvidzon, S. Maayani, H. Nagar, T. Admon, V. Shuvayev, L. Yang, L. Deych, Y. Roichman, and T. Carmon, "Toward transformable photonics: Reversible deforming soft cavities, controlling their resonance split and directional emission," *APL Photonics*, vol. 6, p. 071304, July 2021.

[31] A. Lee, P. Zhang, Y. Xu, and S. Jung, "Radiation pressure-induced nonlinearity in a micro-droplet," *Optics Express*, vol. 28, p. 12675, Apr. 2020.

[32] D. McAuslan, G. Harris, C. Baker, Y. Sachkou, X. He, E. Sheridan, and W. Bowen, "Microphotonic Forces from Superfluid Flow," *Physical Review X*, vol. 6, p. 021012, Apr. 2016.

[33] H. London, "Thermodynamics of the thermomechanical effect of liquid He II," *Proceedings of the Royal Society of London. Series A, Mathematical and Physical Sciences*, pp. 484–496, 1939.

[34] C. Enss and S. Hunklinger, *Low-Temperature Physics*. Springer, Apr. 2005.

[35] J. F. Allen and H. Jones, "New phenomena connected with heat flow in helium II," *Nature*, vol. 141, no. 3562, pp. 243–244, 1938.

[36] M. A. Weilert, D. L. Whitaker, H. J. Maris, and G. M. Seidel, "Laser levitation of superfluid helium," *Journal of Low Temperature Physics*, vol. 98, pp. 17–35, Jan. 1995.

[37] K. R. Atkins, B. Rosenbaum, and H. Seki, "Evaporation Effects during Superflow of Liquid Helium II," *Physical Review*, vol. 113, pp. 751–754, Feb. 1959.

[38] F. M. Ellis and H. Luo, "Observation of the persistent-current splitting of a third-sound resonator," *Physical Review B*, vol. 39, no. 4, p. 2703, 1989.

[39] A. M. R. Schechter, R. W. Simmonds, R. E. Packard, and J. C. Davis, "Observation of 'third sound' in superfluid ^3He ," *Nature*, vol. 396, pp. 554–557, Dec. 1998.

[40] C. G. Baker, G. I. Harris, D. L. McAuslan, Y. Sachkou, X. He, and W. P. Bowen, "Theoretical framework for thin film superfluid optomechanics: towards the quantum regime," *New Journal of Physics*, vol. 18, p. 123025, Dec. 2016.

[41] M. Poot, K. Y. Fong, M. Bagheri, W. H. P. Pernice, and H. X. Tang, "Backaction limits on self-sustained optomechanical oscillations," *Physical Review A*, vol. 86, p. 053826, Nov. 2012. Publisher: American Physical Society.

[42] H. Choi, M. Heuck, and D. Englund, "Self-Similar Nanocavity Design with Ultrasmall Mode Volume for Single-Photon Nonlinearities," *Physical Review Letters*, vol. 118, p. 223605, May 2017.

[43] E. Gil-Santos, C. Baker, D. T. Nguyen, W. Hease, C. Gomez, A. Lemaître, S. Ducci, G. Leo, and I. Favero, "High-frequency nano-optomechanical disk resonators in liquids," *Nature Nanotechnology*, vol. 10, pp. 810–816, Sept. 2015.

[44] P. Kittel, "Orbital resupply of liquid helium," *Journal of Spacecraft and Rockets*, vol. 23, pp. 391–396, July 1986.

[45] S. Kurihara, "Large-amplitude quasi-solitons in superfluid films," *Journal of the Physical Society of Japan*, vol. 50, no. 10, pp. 3262–3267, 1981.

[46] A. Ashkin and J. M. Dziedzic, "Radiation Pressure on a Free Liquid Surface," *Physical Review Letters*, vol. 30, pp. 139–142, Jan. 1973.

[47] C. Monat, P. Domachuk, and B. J. Eggleton, "Integrated optofluidics: A new river of light," *Nature Photonics*,

vol. 1, pp. 106–114, Feb. 2007.

[48] R. Dahan, L. L. Martin, and T. Carmon, “Droplet optomechanics,” *Optica*, vol. 3, p. 175, Feb. 2016.

[49] I. S. Maksymov and A. D. Greentree, “Coupling light and sound: giant nonlinearities from oscillating bubbles and droplets,” *Nanophotonics*, vol. 8, pp. 367–390, Mar. 2019.

[50] J. Rosenberg, Q. Lin, and O. Painter, “Static and dynamic wavelength routing via the gradient optical force,” *Nature Photonics*, vol. 3, pp. 478–483, Aug. 2009.

[51] C. Sun, M. Wade, M. Georgas, S. Lin, L. Alloatti, B. Moss, R. Kumar, A. H. Atabaki, F. Pavanello, J. M. Shainline, J. S. Orcutt, R. J. Ram, M. Popović, and V. Stojanović, “A 45 nm CMOS-SOI Monolithic Photonics Platform With Bit-Statistics-Based Resonant Microring Thermal Tuning,” *IEEE Journal of Solid-State Circuits*, vol. 51, pp. 893–907, Apr. 2016.

[52] X. He, C. Baker, Y. Sachkou, A. Sawadsky, S. Forstner, Y. Sfendla, and W. Bowen, “Phonon Confinement by the Force of Light,” in *CLEO Pacific Rim Conference*, (Hong Kong), p. Tu3F.3, OSA, 2018.

[53] A. B. Matsko and V. S. Ilchenko, “Optical resonators with whispering-gallery modes-part I: basics,” *IEEE Journal of Selected Topics in Quantum Electronics*, vol. 12, pp. 3–14, Jan. 2006.

[54] D. R. Tilley and J. Tilley, *Superfluidity and Superconductivity*. CRC Press, Jan. 1990.

[55] A. D. Kashkanova, A. B. Shkarin, C. D. Brown, N. E. Flowers-Jacobs, L. Childress, S. W. Hoch, L. Hohmann, K. Ott, J. Reichel, and J. G. E. Harris, “Superfluid Brillouin optomechanics,” *Nature Physics*, vol. 13, pp. 74–79, Jan. 2017.

[56] A. Shkarin, A. Kashkanova, C. Brown, S. Garcia, K. Ott, J. Reichel, and J. Harris, “Quantum Optomechanics in a Liquid,” *Physical Review Letters*, vol. 122, p. 153601, Apr. 2019.

[57] G. I. Harris, A. Sawadsky, Y. L. Sfendla, W. W. Wasserman, W. P. Bowen, and C. G. Baker, “Proposal for a quantum traveling Brillouin resonator,” *Optics Express*, vol. 28, pp. 22450–22461, July 2020. Publisher: Optical Society of America.

[58] F. Souris, X. Rojas, P. Kim, and J. Davis, “Ultralow-Dissipation Superfluid Micromechanical Resonator,” *Physical Review Applied*, vol. 7, p. 044008, Apr. 2017.

[59] L. Ding, C. Baker, P. Senellart, A. Lemaitre, S. Ducci, G. Leo, and I. Favero, “High Frequency GaAs Nano-Optomechanical Disk Resonator,” *Physical Review Letters*, vol. 105, Dec. 2010.

[60] R. J. Donnelly and C. F. Barenghi, “The Observed Properties of Liquid Helium at the Saturated Vapor Pressure,” *Journal of Physical and Chemical Reference Data*, vol. 27, pp. 1217–1274, Nov. 1998.

[61] G. Sidebotham, *Heat Transfer Modeling*. Cham: Springer International Publishing, 2015.

[62] G. Swift, T. Molinski, and W. Lehn, “A fundamental approach to transformer thermal modeling. I. Theory and equivalent circuit,” *IEEE Transactions on Power Delivery*, vol. 16, pp. 171–175, Apr. 2001.

[63] J. Altet and A. Rubio, *Thermal Testing of Integrated Circuits*. Boston, MA: Springer US, 2002.

[64] K. J. Kontoleon, “Dynamic thermal circuit modelling with distribution of internal solar radiation on varying façade orientations,” *Energy and Buildings*, vol. 47, pp. 139–150, Apr. 2012.

[65] Y. Gan, J. Wang, J. Liang, Z. Huang, and M. Hu, “Development of thermal equivalent circuit model of heat pipe-based thermal management system for a battery module with cylindrical cells,” *Applied Thermal Engineering*, vol. 164, p. 114523, Jan. 2020.

[66] M. P. Zaitlin and A. C. Anderson, “Phonon thermal transport in noncrystalline materials,” *Phys. Rev. B*, vol. 12, pp. 4475–4486, Nov 1975.

[67] R. C. Zeller and R. O. Pohl, “Thermal conductivity and specific heat of noncrystalline solids,” *Physical Review B*, vol. 4, no. 6, p. 2029, 1971.

[68] G. L. Pollack, “Kapitza resistance,” *Rev. Mod. Phys.*, vol. 41, pp. 48–81, Jan 1969.

[69] E. Long and L. Meyer, “Superfluidity and Heat Transport in the Unsaturated Helium-II Film,” *Physical Review*, vol. 98, no. 6, p. 1616, 1955.

[70] H. Haus, *Waves and fields in optoelectronics*. 1984.

[71] D. Browne, “Nonlinear effects in the damping of third-sound pulses,” *Journal of low temperature physics*, vol. 57, no. 3, pp. 207–226, 1984.

[72] K. R. Atkins and C. E. Chase, “The velocity of first sound in liquid helium,” *Proceedings of the Physical Society. Section A*, vol. 64, pp. 826–833, sep 1951.

[73] “Comsol material library.”

[74] A. K. Raychaudhuri, “Origin of the plateau in the low-temperature thermal conductivity of silica,” *Physical Review B*, vol. 39, pp. 1927–1931, Jan. 1989.

[75] J. Rumble, *CRC handbook of chemistry and physics*. CRC Press llc Boca Raton, FL, 2017.

[76] F. Pobell, *Matter and methods at low temperatures*. Berlin ; New York: Springer, 3rd, rev. and expanded ed. ed., 2007.

[77] W. B. Gauster, “Low-Temperature Grüneisen Parameters for Silicon and Aluminum,” *Physical Review B*, vol. 4, pp. 1288–1296, Aug. 1971.

Acknowledgements

The authors acknowledge the facilities, and the scientific and technical assistance, of the Microscopy Australia Facility at the Centre for Microscopy and Microanalysis (CMM), The University of Queensland.

Contents

References	8
A. Experimental details	11
1. Experimental setup	11
2. Superfluid film thickness	11
3. Calculation of the third sound modes of the microsphere resonator	12
4. Calculation of effective mass, coupling rate and thermal conductance	14
B. Thermal-electric circuit analogy	16
1. Thermal-electric elements of substrate - silica	16
2. Thermal Kapitza resistance at the interface	17
3. Thermal-electric elements of superfluid helium He-II	18
4. Transfer-function for the superfluid helium temperature $V_{\text{He}}(\Omega, T)$	18
5. Thermal response time	22
6. Figure of merit - fountain pressure dynamical backaction optimization	22
C. Numerical model	23
D. Lasing thresholds for various systems	28
E. Thermodynamic efficiency	28
F. Single photon detection	28
1. Comparison to radiation pressure per photon	31
G. Comparison with thermo-elastic stress in a crystal	31

A.

Experimental details

A.

Experimental setup

The microsphere resonator is located in a superfluid-tight sample chamber at the bottom of a Bluefors dilution refrigerator (base temperature 10 mK) [29]. Telecom laser light ($\lambda = 1554$ nm) from a low-noise erbium-doped fiber laser (Koheras ADJUSTIK) is evanescently coupled into the microsphere via a tapered optical fiber [27]. Precise fiber positioning is achieved through Attocube nanopositioning stages. The measurements are performed with the pulse-tube cooler (PTC) turned off in order to minimize vibrations. When the PTC is switched off, substitute cooling power is provided by a liquid helium ‘battery’, containing approximately 1L of liquefied ^4He , located on the 4K stage, providing about 2-3 hours of measurement with the pulse tube off. The sample chamber contains a small volume of alumina nanoparticles in order to increase the effective chamber surface area ($\sim 10 \text{ m}^2$), leading to more precise film thickness control and greater film thickness stability [38]. While at base temperature, ^4He gas can be injected from the top of the cryostat into the sample chamber through a thin capillary, allowing for in situ control of the superfluid film thickness.

A.

Superfluid film thickness

The mean superfluid film thickness d_0 covering the microsphere resonator can be estimated by tracking the optical resonance frequency shift $\Delta\omega_0$ that a whispering gallery mode (WGM) experiences as a superfluid film forms onto the microsphere surface [27, 29]. The film thickness d_0 is then given by $\Delta\omega_0/G$, with $G = \frac{\partial\omega_0}{\partial x}$ the optomechanical coupling rate which describes the optical cavity angular resonance frequency shift per unit deposited superfluid film thickness on the resonator surface [40]. Microsphere resonators support a wide variety of WGM resonances described by their radial, polar and azimuthal mode numbers along with their (TE or TM) polarization [53]. However all these resonances have here a similar coupling strength G (see section A 4), such that specific identification of the tracked WGM is not required.

An additional means to determine the film thickness is available for saturated films, as used in these experiments. As described above, the film is formed and thickened by injecting controlled volumes of ^4He gas into the sample chamber via a capillary. After a certain volume, any additional injected ^4He gas leaves the WGM resonance frequencies

essentially unaffected. This corresponds to the regime of saturated film [34, 54]¹. At this point the helium pressure in the chamber is equal to the saturated vapor pressure p_0 , and any additional helium gas liquefies into a superfluid reservoir at the lowest point of the sample chamber. In this saturated regime, the film thickness is solely determined by the height z between the microsphere and the reservoir, and can be obtained by equating the van der Waals and gravitational chemical potentials $\mu_{\text{vdW}} = \frac{-\alpha_{\text{vdW}}}{d^3}$ and $\mu_{\text{grav}} = gz$, yielding [34]:

$$d_0 = \sqrt[3]{\frac{\alpha_{\text{vdW}}}{gz}} \quad (\text{A1})$$

Here $\alpha_{\text{vdW}} = 2.6 \times 10^{-24} \text{ m}^5 \text{s}^{-2}$ is the van der Waals coefficient for silica [40] and $g = 9.8 \text{ m.s}^{-2}$ the gravitational acceleration. The latter method is for our system the most precise technique to determine the film thickness.

- The sphere is held at a height $z = 2 \text{ cm} \pm 1 \text{ mm}$ above the lowest point in the sample chamber. In the saturated regime, Eq. (A1) predicts a film thickness of $d_0 = 23.7 \text{ nm} \pm 0.4 \text{ nm}$.
- Using the WGM shift to determine the superfluid film thickness was less precise in these experiments. We observed an optical mode shift of 29 pm after a first helium injection. Using an optomechanical coupling rate $G/2\pi = 0.2 \text{ GHz/nm}$ (see section A 4) this optical shift corresponds to a film thickness $d_0 = 18 \text{ nm}$. Several days later we added more helium in order to better approach the experimental set-point shown in Fig. 2 of the main text and observed a mechanical mode frequency shift of 13 Hz, which suggest an additional film thickness of 2-3 nm, adding up to a total film thickness of $\simeq 21 \text{ nm}$. Since these measurements were done over several days and combine two different techniques, this value has a larger uncertainty.
- A third option to determine the film thickness is using the eigenmode simulations in COMSOL. This is achieved by fitting the measured experimental frequency of the fundamental third sound mode (72 Hz), using the film thickness as fit parameter. This method leads to an estimated film thickness of $\sim 27 \text{ nm}$. This value has an uncertainty of around 3 nm, due to uncertainties in the exact length of the stem which defines the fundamental third sound mode (see section A 3). The glue with which the stem is glued to the holder could affect the length of the stem. A deviation of 400 μm could lead to a film thickness of 24 nm with matching frequency of 72 Hz.

Based on these calculations, we determine the superfluid film thickness to be $24 \text{ nm} \pm 3 \text{ nm}$, which is within the error bars and agrees with all three thickness estimation methods.

A.

Calculation of the third sound modes of the microsphere resonator

Previous experimental work with superfluid third sound resonators mainly employed disk-shaped resonators [27–29, 38, 39], for which analytical expressions (in the form of Bessel modes) exist for the third-sound resonances. While similar expressions exist for spheres (spherical harmonics), none naturally exist for the sound modes confined to the 2D outer surface of an arbitrary 3D geometry, such as the silica microsphere resonator including its supporting stem shown in the SEM micrograph in Fig. 3(a). To address this, we note that the superfluid helium flow in the third sound wave is considered inviscid, irrotational and incompressible². As such it is a potential flow and, in the limit of small wave amplitude, the out-of-plane deflection of the superfluid surface $\eta(\vec{r}, t)$ obeys the simple wave equation:

$$\left(\nabla^2 - \frac{1}{c^2} \frac{\partial^2}{\partial t^2} \right) \eta = 0 \quad (\text{A2})$$

Here c is the speed of sound, which neglecting the influence of surface tension, takes the form $c_3 = \sqrt{3 \frac{\rho_s}{\rho} \frac{\alpha_{\text{vdW}}}{d^3}}$ [40]. Assuming a separable time-harmonic standing wave solution, of the kind $\eta(\vec{r}, t) = \eta(\vec{r}) e^{i\Omega t}$, leads to the Helmholtz equation for the spatial mode profile $\eta(\vec{r})$:

$$(\nabla^2 + k^2) \eta(\vec{r}) = 0, \quad (\text{A3})$$

¹ Differing from the unsaturated regime of our previous works [27, 28, 32].

² Indeed, while superfluid helium is in fact quite compressible [55–57] (with a bulk modulus of approximately 8 MPa compared to 2 GPa for water), the van der Waals pressure exerted on the superfluid helium's film free surface (typically in the kPa range

for the film thicknesses considered here [29]) is approximately three orders of magnitude lower than helium's bulk modulus. As a consequence, any local influx of superfluid predominantly leads to a thickening of the film and not an increase in density, such that the superfluid may be well approximated as incompressible in the third sound wave.

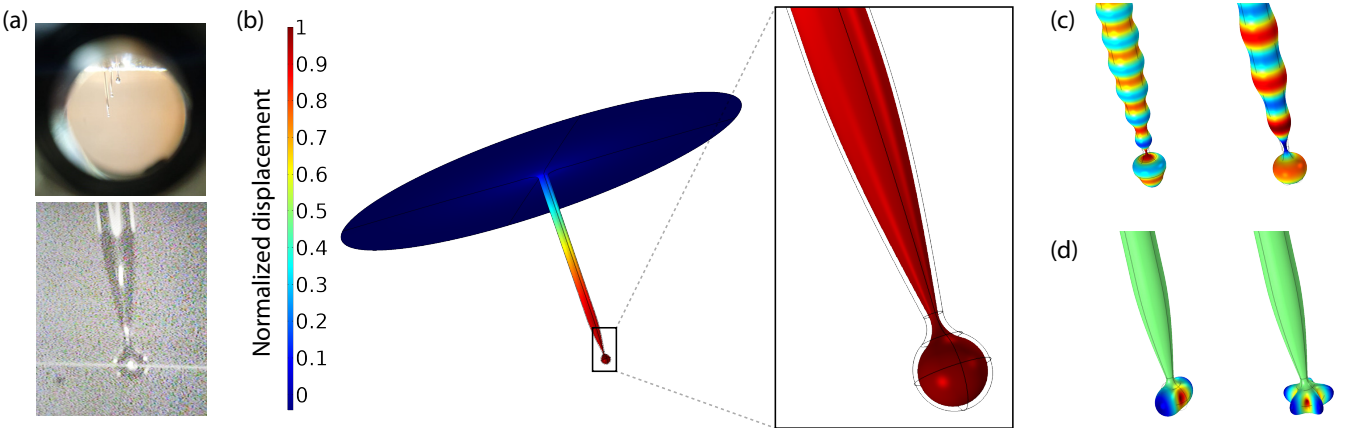


FIG. 6. (a) Top: three microspheres of varying diameter and stem length imaged through the sample chamber window. Bottom: image of the silica microsphere and the coupling tapered fiber, measured at cryogenic temperature with a long working distance microscope objective. (b) Fundamental third sound eigenmode localized to the fiber stem, obtained through finite element simulations. The rapid enlargement of the cross-section represents the point at which the fiber stem is glued to the sample holder. Inset shows how the fluid motion alternatively thins (and thickens) the film around the tip of the sphere. (c) Higher order third sound excitations of the fiber stem and sphere. (d) Third sound modes localized to the microsphere tip, closely resembling the $Y_2^2(\theta, \phi)$ and $Y_5^5(\theta, \phi)$ eigenmodes of an ideal sphere.

where $k^2 = \frac{\Omega^2}{c^2}$ and the displacement profile $\eta(\vec{r})$ is defined on the (2D) surface of the (3D) resonator geometry. When the resonator is a sphere of radius R , the third sound modes are given by the eigenfunctions of the angular part of the Laplacian operator $\Delta = \nabla^2$, called the spherical harmonic functions $Y_m^l(\theta, \phi)$ of degree l and order m , with eigenvalue $k^2 = l(l+1)/R^2$ and frequency:

$$\Omega = kc = \frac{c\sqrt{l(l+1)}}{R}. \quad (\text{A4})$$

Similarly, the third sound modes confined to the surface of an arbitrary three dimensional geometry may be obtained through solving the Helmholtz equation on the exterior 2D surface of this 3D geometry with the help of finite element modelling software (Comsol Multiphysics). We use this technique to obtain the modes of oscillation of a superfluid film confined to the surface of a silica microsphere whispering gallery mode resonator, including its supporting stem. The microsphere resonator is obtained by melting the end of a silica single mode fiber (SMF-28) in a fusion splicer. The non-reflown end of the fiber is then held in place on a sample holder inside the cryostat by a large drop of UV glue (not visible here). Three such resonators, of differing stem length l , are shown in the top panel of Fig. 6(a), protruding from the sample holder in order to allow optical access through a tapered fiber (see bottom panel). Fig. 6(b) shows the fundamental mode of oscillation of a superfluid film confined to the surface of such a silica microsphere resonator. Acoustic confinement is provided by the large change in acoustic impedance at the contact point to the sample holder due to the rapid change in cross-sectional area, much like in a Helmholtz resonator [58]. This is evidenced by the fact that the obtained resonance frequency $\Omega_M/2\pi = \sim 86$ Hz for a 24 nanometer thick film—which reasonably closely matches that observed in the experiments—is essentially independent of the choice of fixed (Dirichlet) or free (von Neumann) boundary condition at the edge of the simulation domain [40]. For this fundamental acoustic resonance, superfluid oscillates back and forth between the surrounding bath and the tip of the sphere, thereby efficiently modulating the whispering gallery mode optical path-length, as shown in the inset of Fig. 6(b). Higher order excitations of the stem and sphere are displayed in Fig. 6(c).

This acoustic confinement through impedance mismatch is also at play at the level of the thin neck which joins the silica microsphere to the silica fiber stem. This results in (higher frequency) third sound modes localized on the spherical tip, as shown in Fig. 6(d), with mode profiles and eigenfrequencies closely matching those given by the spherical harmonic functions $Y_m^l(\theta, \phi)$ describing the eigenmodes of a perfect sphere (see section below).

Sphere modes

In addition to the fundamental stem mode discussed in the main text, we observe a number of high-frequency modes consistent with third sound modes localized on the microsphere itself. Fig. 7 shows a representative spectrum,

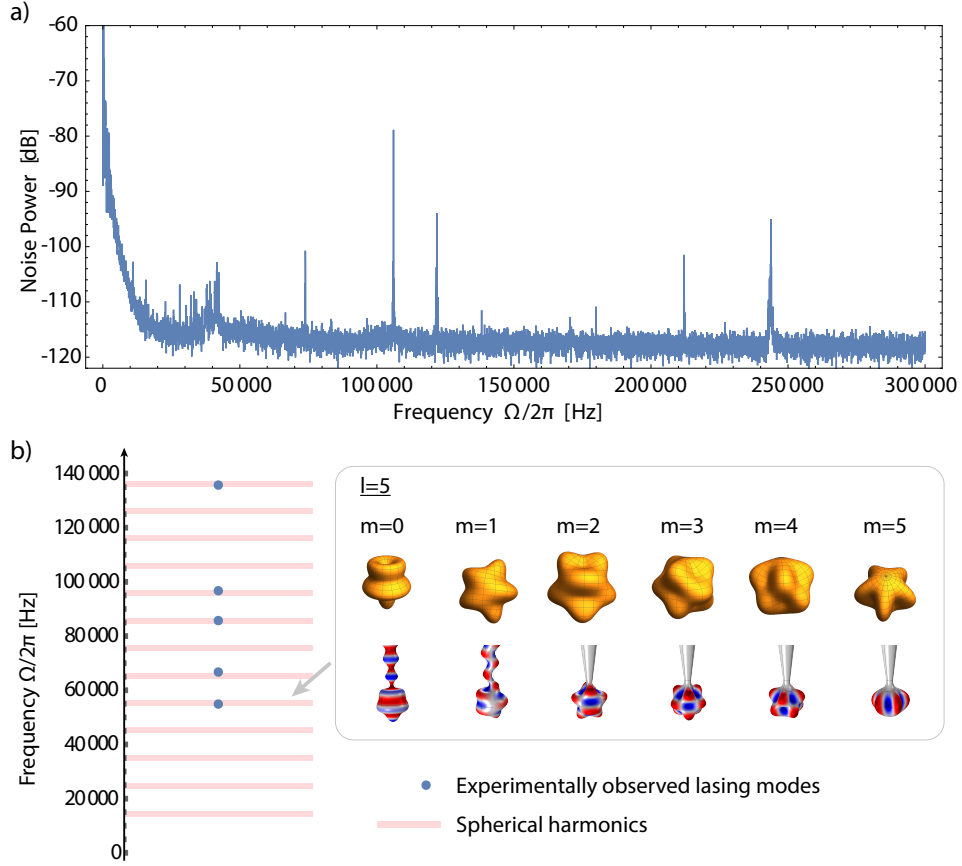


FIG. 7. (a) Power spectrum showing a number of high-frequency third sound modes, acquired with a film thickness of approximately 7.5 nm. (b) Matching of experimentally observed lasing modes (blue dots) to frequency of spherical harmonics Y_m^l of an ideal sphere (see Eq. (A4)), (width of band 2 kHz).

acquired with a film thickness of ~ 7.5 nm. A number of third sound modes are visible with frequencies ranging from tens to hundreds of kHz and Q factors in the 10^4 range. These modes can be brought into regenerative oscillation with nanowatts of optical power. Which particular mode experiences dynamical backaction is strongly dependent on laser-cavity detuning. Fig. 7(b) records the frequencies of the third sound modes which could be brought into lasing during an experimental run. Both their density and frequency are consistent with spherical harmonics Y_m^l of an ideal sphere (pink bands, where l is incremented from 1 to 13). More precise mode identification was not performed here, as identifying the mode frequency provides information only on the degree l (see Eq. A4), and spherical harmonics of degree l have $2l + 1$ degeneracy (the order m can take integer values from $-l$ to l). This is illustrated in the inset of Fig. 7(b), which displays the analytical spherical harmonic modes of an ideal sphere $Y_m^l(\theta, \phi)$, along with the corresponding eigenmodes of the sphere with stem obtained through finite element simulation (negative values of m which rotate the eigenmode are not shown here).

A.

Calculation of effective mass, coupling rate and thermal conductance

Optomechanical coupling G

Calculating the optomechanical coupling G requires identification of the employed WGM in order to compute its field overlap with the superfluid coating the resonator [40]. However, microspheres have a very dense whispering gallery mode spectrum, with WGMs differing by their radial, polar and azimuthal mode orders (n , l and m respectively), along with their TE or TM polarization [53], as illustrated in Fig. 8(a). This large WGM mode density makes it difficult to identify the mode used in the experiments. Fortunately, changes in the WGM order have only a modest influence on the coupling strength, with a $< 1\%$ change arising from incrementing the radial or polar order beyond the fundamental mode (see Fig. 8(a)). A larger difference, on the order of 5%, arises between TE and TM polarizations. Indeed, the WGMs with a dominant radial E field component have a larger field at the surface due to the orthogonal E field discontinuity at the silica interface [40]. Calculation for 100 WGMs closest in resonance wavelength to 1550

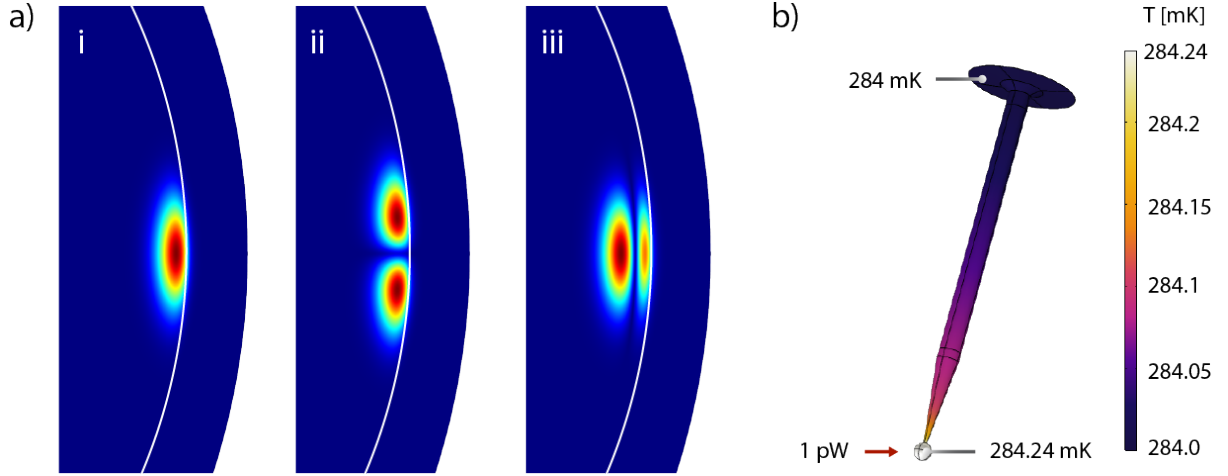


FIG. 8. (a) Whispering gallery modes of a $55\ \mu\text{m}$ radius microsphere resonator, obtained through finite element simulation. i) Fundamental radial $n = 1$ and polar $l = 1$ WGM with azimuthal number $m = 320$ and resonance wavelength $\lambda_0 = 1506\ \text{nm}$. Its optomechanical coupling strength calculated through FEM [40] is $G/2\pi = 1.883 \times 10^{17}\ \text{Hz/m}$. ii) Higher order polar WGM ($n = 1; l = 2; m = 320$), with optomechanical coupling strength $G/2\pi = 1.889 \times 10^{17}\ \text{Hz/m}$. iii) Higher order radial WGM ($n = 2; l = 1; m = 320$), with $G/2\pi = 1.903 \times 10^{17}\ \text{Hz/m}$. (b) Calculation of the thermal conductance of the microsphere resonator. An absorbed power of 1 pW at the level of the spherical tip leads to a steady-state temperature increase by 0.24 mK, corresponding to a thermal conductance $G_{\text{th}} = 4.1 \times 10^{-9}\ \text{W/K}$ at a thermal bath temperature of 284 mK. Physical parameters used in the simulation are summarized in Table III.

nm shows that their G is bounded between 1.9×10^{17} and $2.1 \times 10^{17}\ \text{Hz/m}$, allowing us to constrain the uncertainty to within $\sim 10\%$. These calculated values are in good agreement with the analytical expression for a circular WGM resonator $G = -\frac{\omega_0}{R}$ [59], corrected for the lower dielectric permittivity of superfluid helium [40]:

$$G = \frac{\partial \omega_0}{\partial x} \simeq -\frac{\omega_0}{R} \left(\frac{1 - \varepsilon_{\text{sf}}}{1 - \varepsilon_{\text{SiO}_2}} \right), \quad (\text{A5})$$

which predicts $G/2\pi = 1.93 \times 10^{17}\ \text{Hz/m}$ for a $55\ \mu\text{m}$ radius sphere. Here $\varepsilon_{\text{sf}} = 1.058$ is the relative permittivity of superfluid helium [60], and $\varepsilon_{\text{SiO}_2} = 2.1$ that of silica. We note the value of G is calculated with a radius of $55\ \mu\text{m}$, obtained by an optical microscope measurement. Elsewhere a value of $49.5\ \mu\text{m}$ obtained by SEM is used. This discrepancy is due to the oblate shape of the reflowed microsphere.

Effective mass

The effective mass of an acoustic mode taken at a reduction point \vec{R} is obtained by reducing the system to a point mass m_{eff} moving with velocity $v(\vec{R})$ possessing the same kinetic energy E_k as the original system, that is $m_{\text{eff}} = \frac{2E_k}{v(\vec{R})^2}$. For a third sound mode, this takes the form [40]:

$$m_{\text{eff}} = \frac{2E_p}{v^2(\vec{R})} = \frac{2 \iint \frac{3\rho\alpha_{\text{vdW}}\eta^2(\vec{r})d^2(\vec{r})}{2d^4}}{\eta^2(\vec{R})\Omega^2}, \quad (\text{A6})$$

where $E_p = E_k$ is the potential energy stored in the third sound wave, and the integral is taken over the surface \mathcal{A} of the resonator. For the fundamental mode of the sphere and stem shown in Fig. 6(b), with a reduction point on the equator of the microsphere and a $24\ \text{nm}$ film thickness, $m_{\text{eff}} = 5.1 \times 10^{-3}\ \text{kg}$. Note that this value is approximately 2 billion times larger than the total mass of superfluid covering the resonator $m = \mathcal{A}d\rho_{\text{He}} = 2.65 \times 10^{-12}\ \text{kg}$. The larger effective mass arises from the fact we consider here only the out-of-plane displacement η of the fluid interface (which couples to the light), while the majority of the superflow occurs in plane [40].

electric	thermal	superfluid mass flow
charge $q[A \cdot s]$	heat $Q[J]$	mass $m[kg]$
current $I[A]$	heat flow rate $\dot{Q}[W]$	mass flow rate $\dot{m}[kg/s]$
voltage $V[V]$	temperature $T[K]$	chemical potential $\mu[J/kg]$
resistance $R[V/A]$	heat resistance $R_{th}[K/W]$	-
capacitance $C[A \cdot s/V]$	heat capacitance $C_{th}[J/K]$	mass capacitance $C_m = dm/d\mu[1/J]$
inductance $L[H]$	-	mass inductance $L_m[m^2/kg]$
$I = \Delta V/R$	$\dot{Q} = \Delta T/R_{th}$	-
$I = CdV/dt$	$\dot{Q} = C_{th}dT/dt$	$\dot{m} = C_m d\mu/dt$
Kirchoff's current law	first law of thermodynamics	law of conservation of mass

TABLE I. Electric, thermal and superfluid mass flow analog quantities.

Radiation pressure Single photon optomechanical coupling rate $g_{0_{rp}}$

For the low-frequency stem mode shown in Fig. 6b, the superfluid displacement is uniform along the tip of the microsphere where the light is confined, such that the radiation pressure single photon optomechanical coupling rate $g_{0_{rp}}$ is given by [10, 40]:

$$g_{0_{rp}} = Gx_{zpf} = G\sqrt{\frac{\hbar}{2m_{\text{eff}}\Omega}}. \quad (\text{A7})$$

With $G/2\pi = 2 \times 10^{17}$ Hz/m (see section A 4) and $m_{\text{eff}} = 5.1 \times 10^{-3}$ kg (see section A 4), this yields $x_{zpf} = 4.8 \times 10^{-18}$ m and $g_{0_{rp}}/2\pi = 0.95$ Hz.

B.

Thermal-electric circuit analogy

The fountain pressure in superfluid helium is given by [33]:

$$P_{\text{fp}} = \rho_{\text{He}} S_{\text{He}}(T) \Delta T_{\text{He}}, \quad (\text{B1})$$

where ρ_{He} is the superfluid helium density, $S_{\text{He}}(T)$ is the temperature-dependent entropy of helium, and $\Delta T_{\text{He}} = T_{\text{He}} - T$ is the difference between the environment temperature T and the superfluid film covering the resonator at temperature T_{He} . When calculating the fountain pressure force the challenge is to precisely estimate the temperature rise in the superfluid film, because it strongly depends on the thermal parameters of the system (thermal conductivity, specific heat, Kapitza resistance, vapor pressure etc), which in turn are all strongly temperature-dependent. To model this system we use the technique of the thermal-electric analogy.

The thermal-electric analogy as a lumped-element model is a well known approach to analyse and simulate a variety of complex thermal systems [61, 62]. Applications of thermal equivalent circuits range from designing heat sinks for semiconductor circuits [63] and understanding the impact of solar radiation on building energy consumption [64] to battery pack thermal management [65]. Here we use the analogy between thermal quantities and electric quantities (summarized in Table I) to transform our thermal system into an electric circuit analog. In figure 9 a) we show a schematic of our thermal system with the equivalent electric quantities and in b) the electric circuit as an analog representation of our thermal system. The heat source in our system is the absorbed intracavity optical power in the silica sphere, which is represented by the current source I_{ph} in the circuit. There are two paths for the heat flow towards the thermal bath (dark grey). First it can flow through the substrate itself, i.e. the silica stem which is thermally anchored to the cryostat (beige colored area). Second it may flow through the silica/superfluid interface (striped line) with interfacial resistance R_K into the superfluid helium (light blue color) and dissipate via evaporation. Because the heat can dissipate through both paths simultaneously, these are arranged in parallel in the electric circuit. The two main quantities we are interested in are the temperature changes in the substrate ΔT_{sub} and in the superfluid helium thin film ΔT_{He} with respect to the thermal bath. These two quantities are represented by the two thermal potentials (electric analogy: voltage) V_{sub} and V_{He} with respect to some reference voltage, which is the thermal bath (electric analogy: ground). They depend on the thermal resistances R_{th} , capacitance C_{th} , thermal bath temperature T and heat flow rate given by the absorb photons, which is the current I_{ph} in the electric analogy. Knowing these values, we eventually can calculate the fountain pressure and force.

B.

Thermal-electric elements of substrate - silica

In a lumped-element model for heat transfer an element with a non-zero heat capacity is modeled by two quantities in a parallel configuration: a thermal resistance $R_{\text{th-sub}}$ and a thermal capacitance $C_{\text{th-sub}}$ which accounts for the element's thermal inertia.

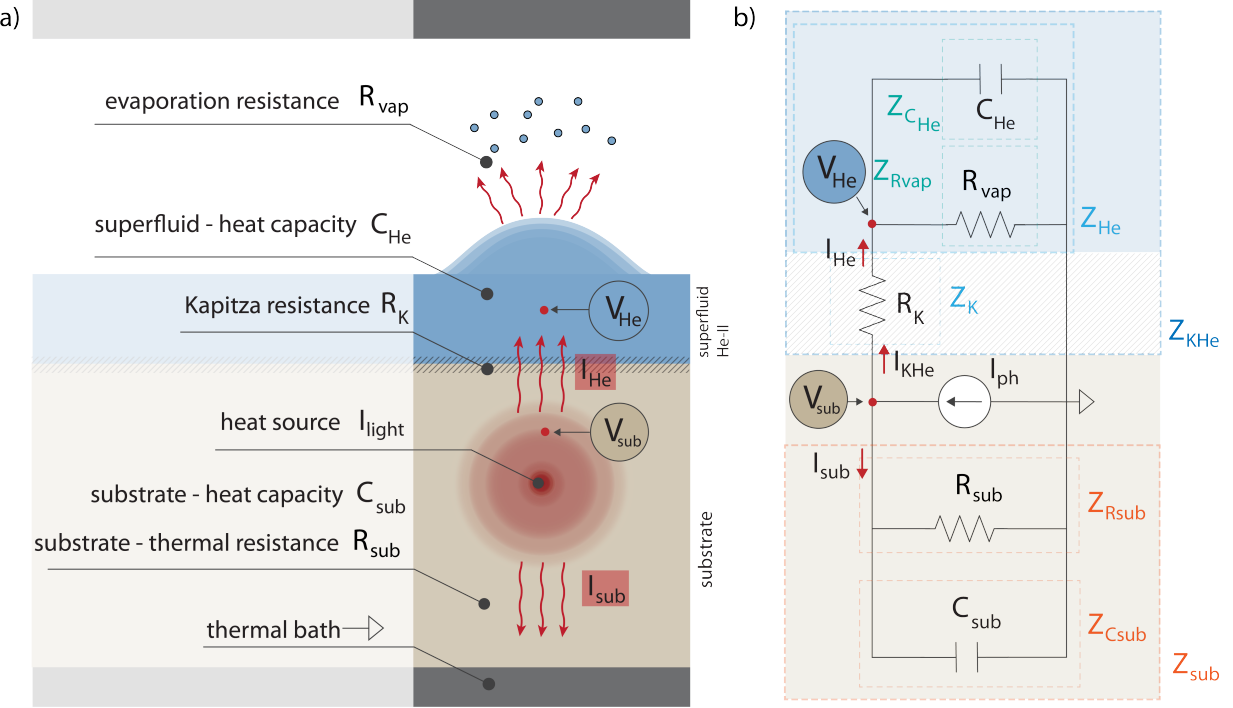


FIG. 9. **Electric-thermal analogy scheme.** a) shows the schematic of our thermal system with the analog electric quantities. The analogy for the heat source (absorbed intra cavity power) is a current source I_{light} and the electric ground represents the thermal bath of the system. b) Electric circuit analogy of our thermal system. The voltages V_{sub} and V_{He} are the analogs of the temperatures in the substrate and the superfluid film.

The thermal resistance R_{sub} can be simulated with COMSOL. All parameters used in this simulation are provided in Table III and are for the bath temperature of 284 mK. Fig. 8(b) shows the steady-state temperature increase in the microsphere plus stem system with $\dot{Q} = 1 \text{ pW}$ of optical power absorbed at the level of the microsphere. The 0.24 mK temperature increase corresponds to a thermal resistance $R_{\text{th-sub}} = 2.44 \times 10^8 \text{ K/W}$ and a thermal conductance $G_{\text{th-sub}} = R_{\text{th-sub}}^{-1} = \kappa_{\text{SiO}_2} @ 284 \text{ mK} \times \phi = 4.1 \times 10^{-9} \text{ W/K}$, where $\kappa_{\text{SiO}_2} @ 284 \text{ mK} = 1.6 \times 10^{-3} \text{ W/m/K}$ is the thermal conductivity for silica at 284 mK and $\phi = 2.52 \times 10^{-6} \text{ m}$ is a temperature-independent geometrical factor (which we obtain from this simulation). The thermal conductivity of silica $\kappa_{\text{SiO}_2}(T)$ is temperature dependent. In figure 10 a) we fitted a function of the form $\kappa_{\text{SiO}_2}(T) = 0.0000488638 \times T + 0.0212904 \times T^2 - 0.00436582 \times T^3 - 0.000101651 \times T^4$ to the data from [66] to get a temperature-dependent thermal resistance of the silica microsphere $R_{\text{th-sub}}(T) = (\kappa_{\text{SiO}_2}(T) \times \phi)^{-1}$.

The thermal capacitance of the substrate is given by $C_{\text{th-sub}} = c_{\text{SiO}_2}(T) \times m_{\text{sub}}$, with m_{sub} being the mass of the microsphere (incl. stem) and $c_{\text{SiO}_2}(T) = 0.00105 \times T + 0.0018 \times T^3$ is the temperature-dependent specific heat capacity for silica (see figure 10 b)), which is a fit function to the data from [67].

B.

Thermal Kapitza resistance at the interface

The interface between the silica and the superfluid thin-film results in an interfacial thermal resistance called the Kapitza resistance. It is temperature and material dependent, and arises due to the large acoustic impedance mismatch between silica and superfluid helium, reducing phonon propagation from one medium to the other. According to [68] the Kapitza resistance has the functional form:

$$R'_K(T) = \frac{15\hbar^3 \rho_{\text{SiO}_2} c_{t_{\text{SiO}_2}}^3}{2\pi^2 k_B^4 \rho_{\text{He}} c_{1_{\text{He}}} F\left(\frac{c_{l_{\text{SiO}_2}}}{c_{t_{\text{SiO}_2}}}\right) T^3}, \quad (\text{B2})$$

where ρ_{SiO_2} and ρ_{He} are the densities of silica and liquid helium, $c_{t_{\text{SiO}_2}}$ and $c_{l_{\text{SiO}_2}}$ are respectively the transverse and longitudinal sound velocities of silica, $c_{1_{\text{He}}}$ is the first sound speed in superfluid helium and $F(c_{l_{\text{SiO}_2}}/c_{t_{\text{SiO}_2}}) = 2.5$ [68] is a silica specified function. Fig. 10 c) shows the temperature dependency of the Kapitza resistance for a silica and superfluid helium interface with units [m²K/W]. When calculating the Kapitza interfacial thermal resistance in our

thermal-electric quantity	functional form	frequency domain
substrate thermal resistance	$R_{\text{sub}}(T) = (\kappa_{\text{SiO}_2}(T)\phi)^{-1}$	$Z_{R_{\text{sub}}}(T) = R_{\text{sub}}(T)$
substrate thermal capacitance	$C_{\text{sub}}(T) = c_{\text{SiO}_2}(T)m_{\text{sub}}$	$\tilde{Z}_{C_{\text{sub}}}(\Omega, T) = \frac{1}{i\Omega C_{\text{sub}}(T)}$
Kapiza Resistance	$R_K(T) \simeq \frac{3h^3 \rho_{\text{SiO}_2} c_{\text{SiO}_2}^3}{\pi^2 k_B^4 \rho_{\text{He}} c_{\text{He}} T^3 \mathcal{A}}$	$Z_K(T) = R_K(T)$
superfluid He thermal resistance	$R_{\text{vap}}(T) = \left(\gamma \sqrt{\frac{m_{\text{He}_{\text{mol}}}}{2\pi RT}} \left(\frac{dP_V}{dT} \right)_{\text{v.p.c}} L_{\text{He}}(T) \mathcal{A} \right)^{-1}$	$Z_{R_{\text{vap}}}(T) = R_{\text{vap}}(T)$
superfluid He thermal capacitance	$C_{\text{He}}(T) = c_{\text{He}}(T)m_{\text{He}}$	$\tilde{Z}_{C_{\text{He}}}(\Omega, T) = \frac{1}{i\Omega C_{\text{He}}(T)}$

TABLE II. Thermal-electric quantities in DC and frequency domain.

system R_K , we need to normalize it to the silica microsphere surface area, i.e. $R_K(T) = R'_K(T)/\mathcal{A}$ [K/W].

B.

Thermal-electric elements of superfluid helium He-II

The superfluid helium thin-film is represented by the thermal resistance R_{vap} and the thermal capacitance C_{He} . In thin superfluid films, the normal fluid component is viscously clamped to the substrate and does not flow. Only the superfluid component, which carries no entropy, is free to move. Thermal conductance through the liquid itself is therefore negligible, and the thermal conductivity occurs primarily through influx of superfluid, which evaporates extracting the latent heat of vaporization [69]. To calculate the thermal conductance $G_{\text{vap}}(T)$ resulting from this evaporative process at a temperature T , we need to multiply the resulting net helium mass flow rate per unit area \dot{m}_{He} by the latent heat of vaporization of helium $L_{\text{He}}(T)$ and divide by the temperature change $(T_0 - T)$, which gives the area-normalized ‘net’ energy leaving due to evaporation. Multiplying by the silica microsphere area \mathcal{A} gives the total evaporative thermal conductance of our superfluid film:

$$G_{\text{vap}}(T) = \dot{m}_{\text{He}} \frac{L_{\text{He}}(T)}{(T_0 - T)} \mathcal{A}. \quad (\text{B3})$$

The net mass flow rate per unit area is given by [25]:

$$\dot{m}_{\text{He}}(T) = \gamma \sqrt{\frac{m_{\text{He}_{\text{mol}}}}{2\pi RT}} \left(\frac{dP_V}{dT} \right)_{\text{v.p.c}} (T_0 - T), \quad (\text{B4})$$

with $\gamma = 1$, $m_{\text{He}_{\text{mol}}}$ as the molar mass of helium, $R = 8.3145 \text{ J mol}^{-1} \text{ K}^{-1}$ the ideal gas constant and $(\frac{dP_V}{dT})_{\text{v.p.c}}$ the gradient of the vapour pressure curve for helium. The saturated vapour pressure $P_V(T)$ curve is plotted in Fig. 10 e), and given by [60]:

$$P_V(T) = \exp(i_0 - \frac{L_0}{RT} + \frac{5}{2} \log(T)), \quad (\text{B5})$$

where $i_0 = 12.2440$ and $L_0 = 59.83 \text{ J/mol}$ is the latent heat of vaporization at absolute zero. The temperature-dependent latent heat of vaporization of helium $L_{\text{He}}(T)$ is an interpolation function, shown in Fig. 10 f), to the data extracted from [60]. The equations B3,B4,B5 all together enable us to derive a temperature-dependent expression for the thermal resistance via evaporation $R_{\text{vap}}(T) = (G_{\text{vap}}(T))^{-1}$.

The temperature-dependent heat capacity of thin-film superfluid helium is given by $C_{\text{He}}(T) = c_{\text{He}}(T)m_{\text{He}}$, with m_{He} being the superfluid helium mass covering the full microsphere (incl. stem) and $c_{\text{He}}(T)$ an interpolation of the temperature-dependent specific heat for superfluid helium, with data obtained from [60] and shown in figure 10 d).

B.

Transfer-function for the superfluid helium temperature $V_{\text{He}}(\Omega, T)$

Having specified the electric analog of each thermal quantity in our system (see sections above) and simplified it to an electric circuit (see figure 9), enables us now to use simple electric calculation techniques to determine the bath-temperature dependent superfluid helium temperature $V_{\text{He}}(\Omega, T)$ and its frequency response (transfer-function) to a fluctuating heat source. This gives us a full framework of our system so we can operate at the ideal temperature and frequency to maximise and control the fountain pressure backaction.

First we transform all thermal-electric quantities into the frequency domain, so they can be written as complex impedances, which are all summarized in table II. The total complex impedance for the substrate and superfluid helium are respectively given by:

$$\tilde{Z}_{\text{sub}}(\Omega, T) = \left(\frac{1}{Z_{R_{\text{sub}}}(T)} + \frac{1}{\tilde{Z}_{C_{\text{sub}}}(\Omega, T)} \right)^{-1} \quad (\text{B6})$$

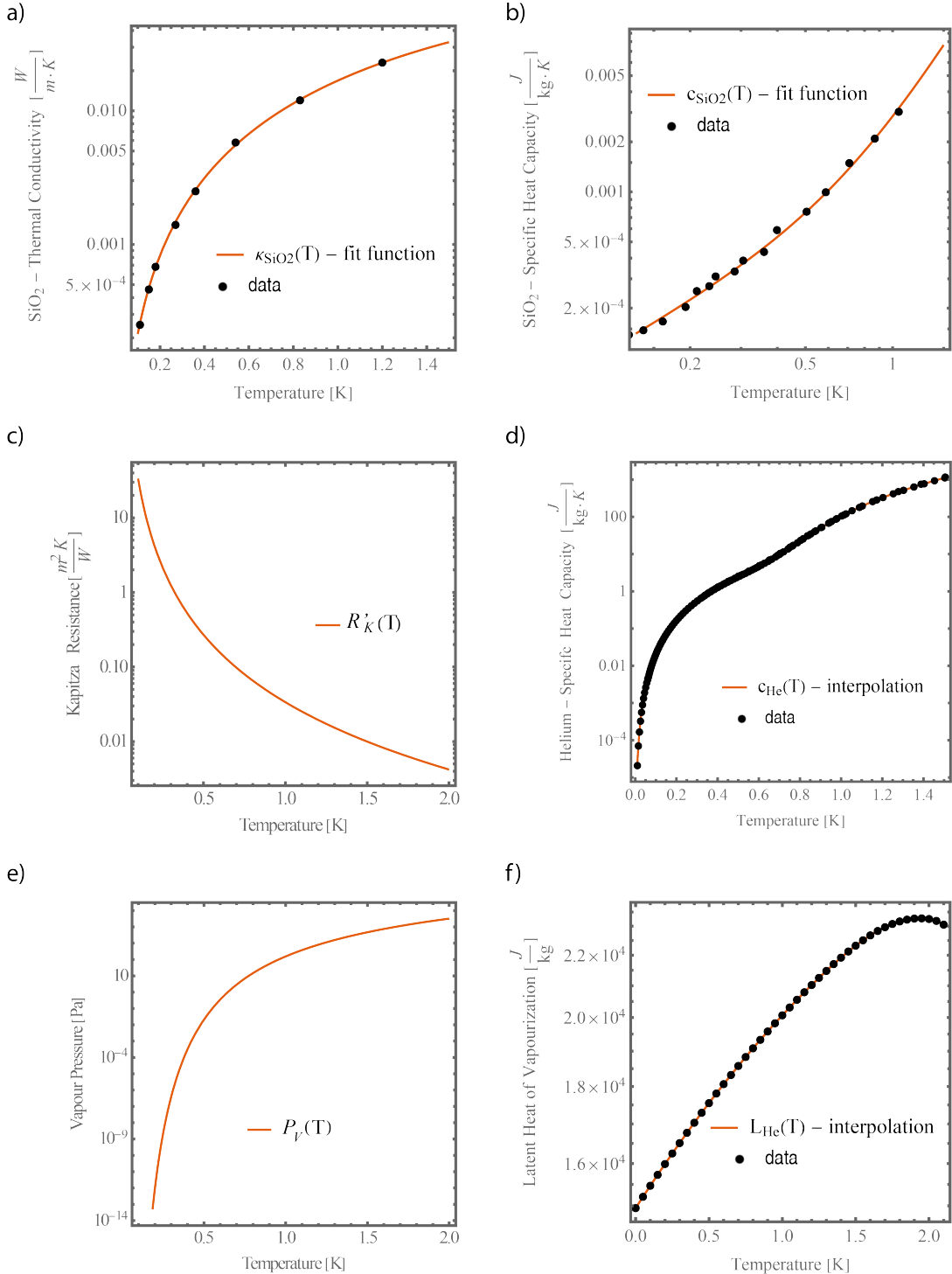


FIG. 10. Temperature-dependent material parameters. Here we present all the temperature-dependent material parameters used for the thermal-electric analogy model. a) Fitted thermal conductivity $\kappa_{\text{SiO}_2}(T)$ of silica with data points taken from literature [66]. b) Fitted specific heat capacity $c_{\text{SiO}_2}(T)$ with measured data from [67]. c) Kapitza resistance of the interface between liquid He-II and silica [68]. The figures d), e) and f) are all helium-related parameters. In d), we show the interpolated specific heat capacity of helium $c_{\text{He}}(T)$ obtained from the data in Ref. [60]. e) plots the vapour pressure for helium, which is given in Ref. [60] in functional form (Eq. B5). In f) $L_{\text{He}}(T)$ is the interpolation of the data for the latent heat of vaporization [60].

and

$$\tilde{Z}_{\text{He}}(\Omega, T) = \left(\frac{1}{Z_{\text{R}_{\text{vap}}}(T)} + \frac{1}{\tilde{Z}_{\text{KHe}}(\Omega, T)} \right)^{-1}. \quad (\text{B7})$$

The combined impedance of superfluid helium and the Kapitza impedance is $\tilde{Z}_{\text{KHe}}(\Omega, T) = \tilde{Z}_{\text{He}}(\Omega, T) + Z_{\text{K}}(T)$, as these two elements are in series, see Fig. 9. This leads to the total impedance of the circuit:

$$\tilde{Z}_{\text{tot}}(\Omega, T) = \left(\frac{1}{\tilde{Z}_{\text{sub}}(\Omega, T)} + \frac{1}{\tilde{Z}_{\text{KHe}}(\Omega, T)} \right)^{-1}. \quad (\text{B8})$$

Therefore the voltage change (thermal realm: temperature) in the substrate is given by Ohm's law:

$$\tilde{V}_{\text{sub}}(\Omega, T) = I_{\text{ph}} \tilde{Z}_{\text{tot}}(\Omega, T). \quad (\text{B9})$$

Considering the temperature drop over the Kapitza resistance, the temperature difference in the superfluid helium can be written as:

$$\begin{aligned} \tilde{V}_{\text{He}}(\Omega, T) &= \tilde{V}_{\text{sub}}(\Omega, T) - V_{\text{K}}(T) \\ &= I_{\text{ph}} \tilde{Z}_{\text{tot}}(\Omega, T) - \tilde{I}_{\text{KHe}}(\Omega, T) Z_{\text{K}}(T). \end{aligned} \quad (\text{B10})$$

The heat flow rate (electric-analogy: current) towards the superfluid helium $\tilde{I}_{\text{KHe}}(\Omega, T)$ is given by Kirchhoff's law as:

$$\tilde{I}_{\text{KHe}}(\Omega, T) = I_{\text{ph}} - \tilde{I}_{\text{sub}}(\Omega, T), \quad (\text{B11})$$

Using equations (B9), (B11) and the relation $\tilde{I}_{\text{sub}}(\Omega, T) = \tilde{V}_{\text{sub}}(\Omega, T) / \tilde{Z}_{\text{sub}}(\Omega, T)$ in equation (B10), results in:

$$\begin{aligned} \tilde{V}_{\text{He}}(\Omega, T) &= I_{\text{ph}} \tilde{Z}_{\text{tot}}(\Omega, T) - \left(I_{\text{ph}} - \frac{I_{\text{ph}} \tilde{Z}_{\text{tot}}(\Omega, T)}{\tilde{Z}_{\text{sub}}(\Omega, T)} \right) Z_{\text{K}}(T) \\ &= I_{\text{ph}} \left(\tilde{Z}_{\text{tot}}(\Omega, T) - Z_{\text{K}}(T) + \frac{Z_{\text{K}}(T) \tilde{Z}_{\text{tot}}(\Omega, T)}{\tilde{Z}_{\text{sub}}(\Omega, T)} \right). \end{aligned} \quad (\text{B12})$$

The voltage here is a complex number. The real temperature increase in the superfluid helium film and the substrate are given by the modulus of the voltage:

$$\Delta T_{\text{He}}(\Omega, T) = V_{\text{He}}(\Omega, T) = |\tilde{V}_{\text{He}}(\Omega, T)| \quad (\text{B13})$$

and

$$\Delta T_{\text{sub}}(\Omega, T) = V_{\text{sub}}(\Omega, T) = |\tilde{V}_{\text{sub}}(\Omega, T)|. \quad (\text{B14})$$

Fig. 11 a) and b) demonstrate $\Delta T_{\text{He}}(\Omega, T)$ and its dependency on the bath temperature T and the drive frequency Ω for an absorbed power of $I_{\text{ph}} = 1 \text{ pW}$, where the red dot displays the operation point of our experimental system. Together with the temperature dependent entropy $S_{\text{He}}(T)$, which is given by an interpolation to some measured data from [60] (see figure 11 c)), the fountain pressure takes the form:

$$P_{\text{fp}}(\Omega, T) = \rho_{\text{He}} S_{\text{He}}(T) \Delta T_{\text{He}}(\Omega, T), \quad (\text{B15})$$

and is plotted in figure 11 d) for the experimental mechanical frequency Ω_{M} . This model shows that our operation temperature of $T = 284 \text{ mK}$ is the optimal temperature that results in the maximum fountain pressure for our system. This maximum arises as a consequence of two competing trends. On one hand, the entropy is an increasing function of T , pointing towards a stronger fountain pressure interaction at higher temperatures (Fig. 11c). On the other hand, the increase in heat capacity and thermal conductivity at higher temperatures reduces the temperature rise ΔT , counteracting the previous effect (Fig. 11b). The fountain pressure force is finally:

$$F_{\text{fp}}(\Omega, T) = P_{\text{fp}}(\Omega, T) \mathcal{A}, \quad (\text{B16})$$

with \mathcal{A} being the surface area of the whole resonator.

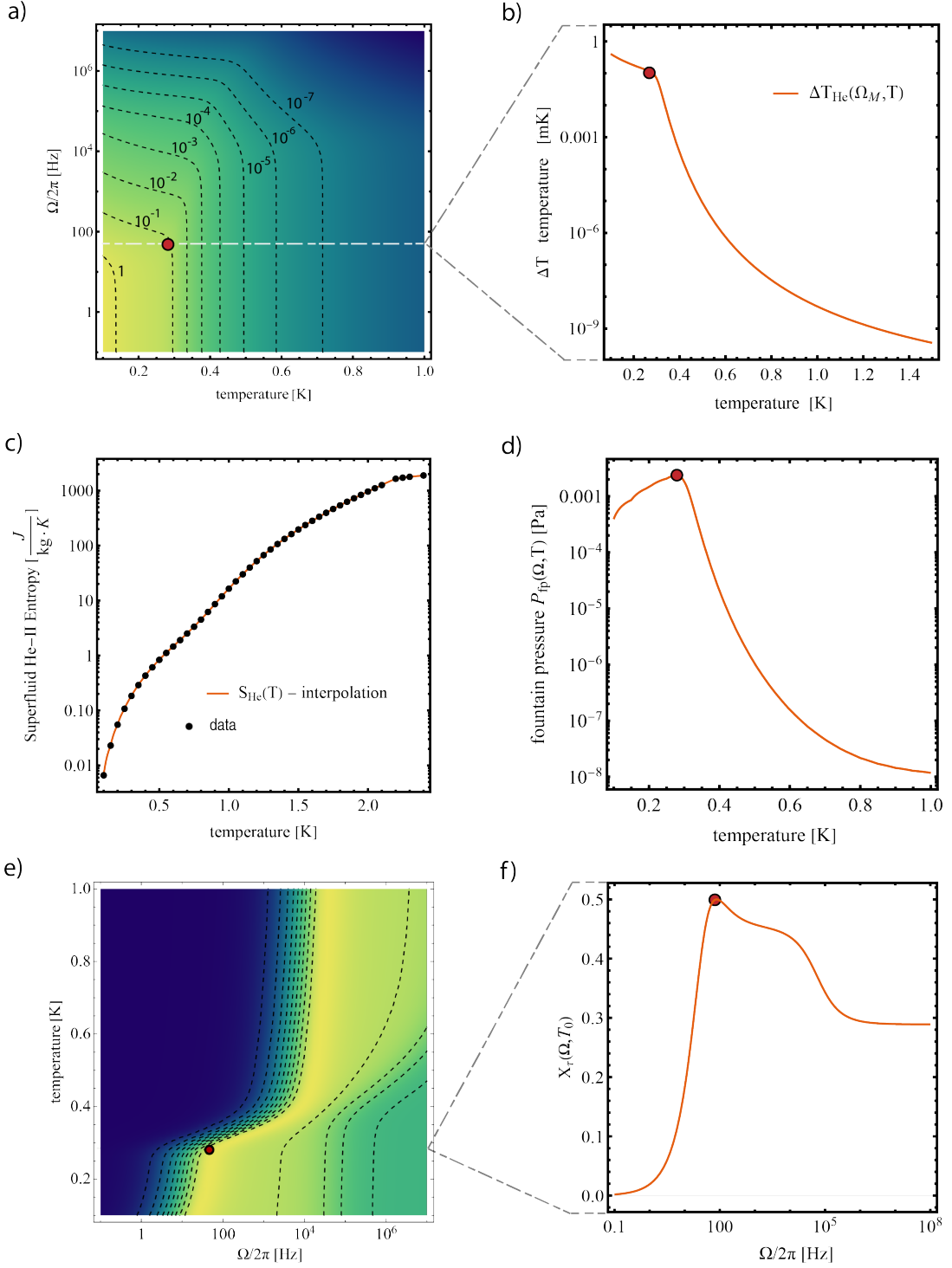


FIG. 11. Modelled transfer functions of the experimental system In all figures the red dot represents the operation point of the experimental system. Figure a) shows a contour-color plot of the superfluid helium temperature increase $\Delta T_{\text{He}}(\Omega, T)$ and its dependency on the thermal bath temperature T and the modulation frequency Ω . b) is a line plot of $\Delta T_{\text{He}}(\Omega_M, T)$ at the experimental mechanical frequency Ω_M . Figure c) shows the interpolation function $S_{\text{He}}(T)$ along with the data of entropy of superfluid helium from [60]. d) plots the superfluid helium fountain pressure $P_{\text{fp}}(\Omega_M, T)$. e) is a contour-color plot of the dynamical backaction function $\chi_{\text{He}}(\Omega, T)$ and f) is a 2D plot of the same function at the given bath temperature $T = 284$ mK.

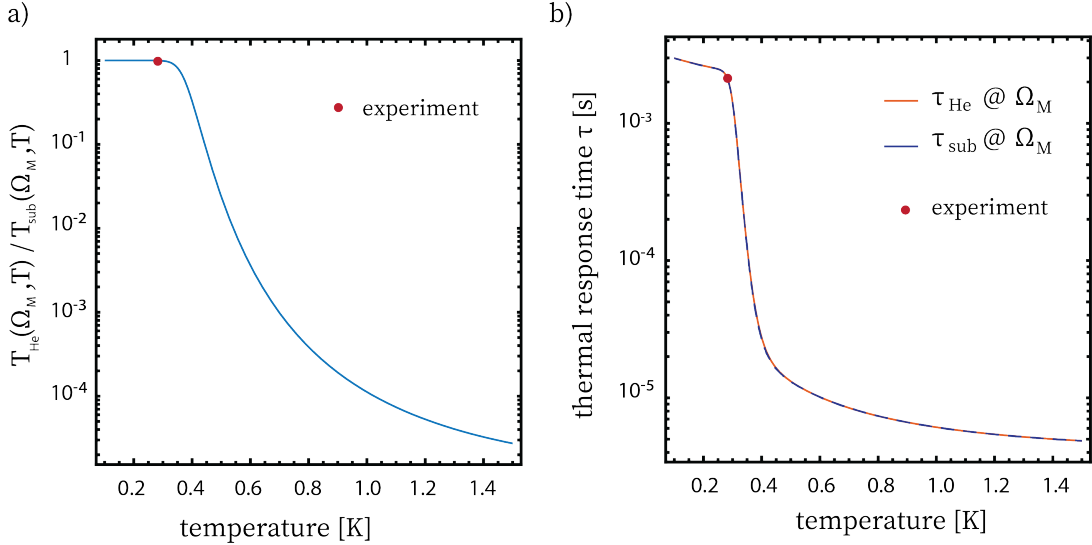


FIG. 12. **Temperature ratio and thermal response time of superfluid helium and the substrate.** At the frequency and temperature used in the experiments (red dot), the temperature of the film closely tracks that of the underlying silica resonator, allowing these to be modelled as a common element in the ODE simulations of section C.

B.

Thermal response time

In addition to maximising $\Delta T_{\text{He}}(\Omega, T)$ to optimise the fountain pressure strength, it is also important to understand and optimize the dynamical backaction efficiency of the system. The theory of photothermal heating and cooling [17, 20] shows that strongest backaction is achieved in the regime $\Omega_M \tau_{\text{th}} \sim 1$, where τ_{th} corresponds to the thermal response time of the superfluid film. The thermal time delay τ_{th} is given by the relation $\tau_{\text{th}} = \phi/\Omega$, with Ω the mechanical frequency and ϕ the phase of the complex transfer function $\tilde{V}_{\text{He}}(\Omega, T)$:

$$\phi_{\text{He}}(\Omega, T) = \arg(\tilde{V}_{\text{He}}(\Omega, T)), \quad (\text{B17})$$

which means that τ_{th} is frequency- and temperature-dependent. The unitless functional form:

$$\chi_{\text{He}}(\Omega, T) = \frac{\Omega \tau_{\text{th}}((\Omega, T))}{1 + (\Omega \tau_{\text{th}}((\Omega, T)))^2}, \quad (\text{B18})$$

represents the optimal time delay of the bolometric forces [16–19]. For $\Omega_M \tau_{\text{th}} \sim 1$ we get $\chi_{\text{He}}(\Omega = 1/\tau_{\text{th}}, T) = 0.5$. Fig. 11 e) shows $\chi_{\text{He}}(\Omega, T)$ in a color-contour plot for our system. Fig. 11 f) is a line cut through (e) for a fixed temperature of 284 mK. The red dot marks the mechanical mode frequency Ω_M of the system, which is at the maximum value of 0.5 for χ_{He} . As a consequence, our choice of superfluid mechanical mode and cryostat temperature allows us to operate at both the optimal point for fountain pressure strength (Fig. 11d), and optimal time-delayed forcing for dynamical backaction (Fig. 11f).

B.

Figure of merit - fountain pressure dynamical backaction optimization

The two main dynamical forces in our system are the fountain pressure force and the radiation pressure force given by:

$$F_{\text{rad}} = n_{\text{cav}} \hbar G, \quad (\text{B19})$$

where n_{cav} is the intracavity photon number, \hbar the reduced Planck constant and G the optomechanical coupling rate. Having the two forces, fountain pressure force and radiation pressure force, and the dynamical backaction efficiency $\chi_{\text{He}}(\Omega, T)$ leads to a figure of merit for the photothermal effect in our system:

$$f_M(\Omega, T) = \frac{F_{\text{fp}}(\Omega, T)}{F_{\text{rad}}} \chi_{\text{He}}(\Omega, T). \quad (\text{B20})$$

C.

Numerical model

Differential equations

The dynamical behaviour of the superfluid resonator may be described by three coupled differential equations relating to the intracavity photon number n_{cav} , the change in mean film thickness at the level of the WGM x and the temperature T . Each of these parameters respectively responds on a characteristic timescale of $1/\kappa \sim \text{ns}$; $\tau_{\text{th}} \sim \text{ms}$ and $1/\Gamma \sim \text{s}$. Since the optical decay rate κ is much larger than all other decay rates, we consider that the intracavity photon number n_{cav} reacts instantaneously to any changes in the cavity (adiabatic limit), such that it takes the steady-state form [11]:

$$|a|^2 = n_{\text{cav}} = \frac{\kappa_{\text{ex}}}{\Delta^2 + \left(\frac{\kappa}{2}\right)^2} \frac{P}{\hbar\omega_L}, \quad (\text{C1})$$

where $\kappa = \kappa_{\text{ex}} + \kappa_i$ is the sum of the extrinsic and intrinsic loss rates respectively [11], and P the laser power at the level of the fiber taper. The detuning Δ is equal to:

$$\Delta = \Delta_0 + Gx \quad \text{with} \quad G = \frac{\partial\omega_0}{\partial x}, \quad (\text{C2})$$

with Δ_0 the cavity detuning for zero displacement and G the optomechanical coupling rate (see section A 4). The dynamics can thus be reduced to two coupled equations of motion. The first determines the motion of the superfluid film:

$$m_{\text{eff}} \ddot{x} + m_{\text{eff}} \Gamma \dot{x} + m_{\text{eff}} \Omega^2 x = F_{\text{fp}} = \rho S(T_0) (T - T_0) \mathcal{A}, \quad (\text{C3})$$

where T_0 and T are respectively the temperature of the environment and that of the superfluid film covering the resonator. This equation, which assumes a constant value for the entropy $S(T_0)$ is valid in the limit $\Delta T \ll T_0$, which is the case in the experiments. The second governs the evolution of the temperature T and arises from conservation of energy:

$$\dot{T} = \frac{n_{\text{cav}} \hbar \omega_L \kappa_i \alpha_{\text{abs}}}{m c} - \frac{G_{\text{th}}(T_0) (T - T_0)}{m c} \quad (\text{C4})$$

Here, $\alpha_{\text{abs}} \in [0, 1]$ corresponds to the fraction of the intrinsic losses dissipated as heat in the resonator, m to the resonator's thermal mass and c its specific heat capacity, and $G_{\text{th}} = \frac{m c}{\tau_{\text{th}}}$ the resonator's thermal conductance. We note here that at the operational point used in the experiments ($\Omega/2\pi = 72$ Hz; $T = 284$ mK) and the low optical powers in the pW range, the superfluid film temperature closely tracks that of the silica microsphere with minimal temperature difference and phase lag (verified through the thermal model of section B, and plotted in Fig. 12). For this reason, in these time-domain numerical simulations, we simplify the thermal system by considering the silica resonator and superfluid film as a common element, of mass m and heat capacity c , dominated by the microsphere mass and heat capacity. This allows us to accurately reproduce the experimental results, as shown below. The time dynamics of our system are obtained by numerically solving the coupled differential equations (Eqs (C3) and (C4)) with an ODE solver (MATLAB software).

Numerical simulations results

Solving these equations with the parameters provided in Table III, we obtain the dynamical behaviour of the superfluid film displacement $\Delta x(t)$, normalized optical output power $|a_{\text{out}}(t)|^2/|a_{\text{in}}(t)|^2$ (where $|a_{\text{out}}(t)|^2$ and $|a_{\text{in}}(t)|^2$ are respectively the output and input optical powers, and are related via input-output formalism [11, 70]) and the temperature fluctuations $\Delta T(t)$ around the environment temperature of $T = 284$ mK. The sub-figures c), d) and e) in figures 13, 14 and 15 show the time-dependency of these parameters in the steady-state phonon lasing regime (i.e. after the initial transient dynamics) at the input powers 3.4 pW, 6.8 pW and 68 pW. The simulations are performed at a cavity detuning where the superfluid film's motional amplitude is maximized (represented by the red dot in sub-figure a)). To appropriately compare the numerical simulations with the measurements, done with a spectrum analyzer and with a heterodyne detection scheme, we added an optical local oscillator field and applied a Fourier transformation to the time-dependent normalized optical output field in the steady state regime of the system for different cavity detunings and optical input powers. The black line in all sub-figures a) of figures 13, 14 and 15 demonstrates the peak value of the fundamental mechanical mode in the normalized spectral density versus cavity detuning for different input powers. This we compared to the normalized amplitudes of the measured mechanical mode at different cavity detunings as well and same input powers, which are displayed as blue dots in all sub-figures a) of figures 13, 14 and 15. The numerical simulation is fitted to the experimental data by using α_{abs} , the fraction of dissipated optical power that gets converted into heat in the resonator, and the mechanical mode decay rate Γ as

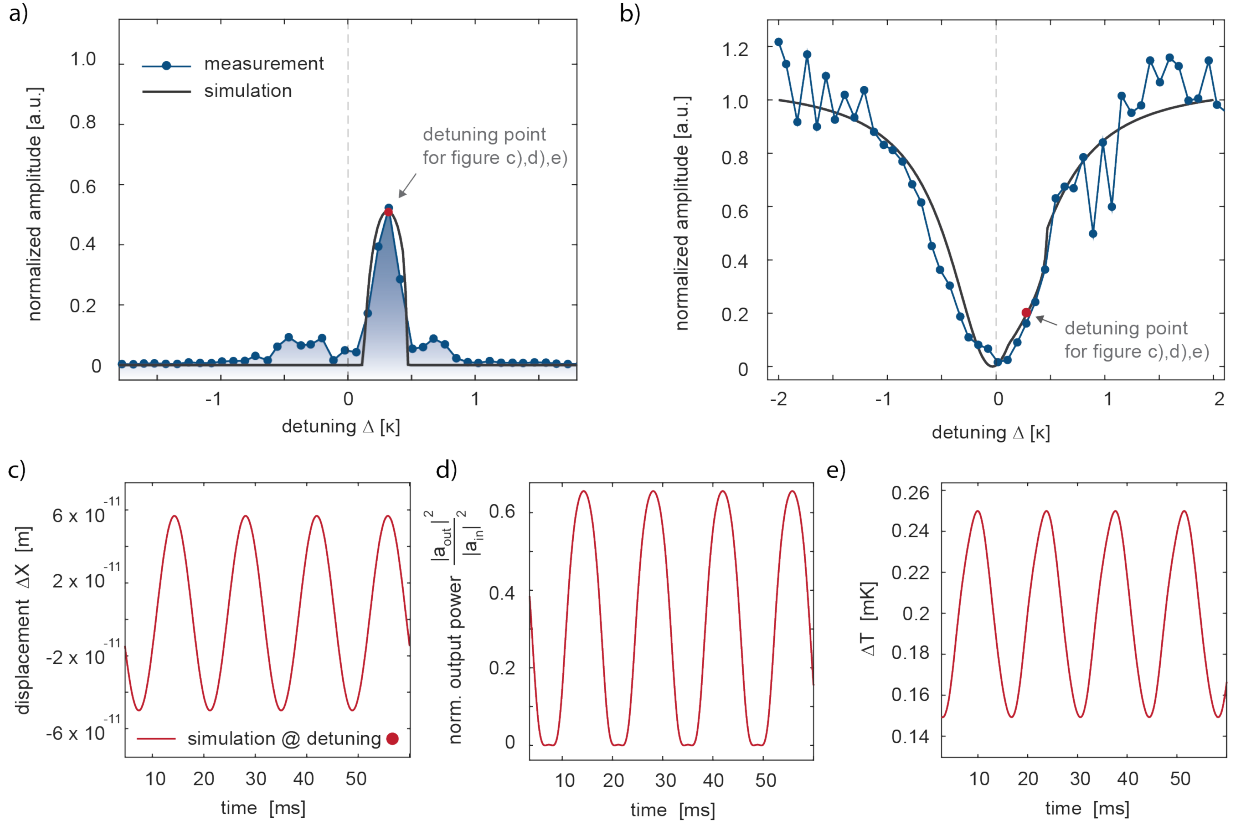


FIG. 13. Numerical simulation for 3.4 pW input power. a) Mechanical mode ($\Omega/2\pi i = 72$ Hz) amplitude as a function of cavity detuning, where the blue dots represent the normalized measured mode peak of the power spectrum and the black line the numerical simulations. b) Normalized optical transmission of the whispering gallery mode resonator depending on the detuning, obtained by plotting the experimentally measured normalized spectral density peak value of the calibration peak at 180 Hz (blue dots) and the local oscillators (80 MHz) normalized spectral density peak value in the numerical simulations (black line). The numerical simulations in c), d) and e) show the time dependency in the steady state regime of respectively the displacement ΔX , the cavity transmitted normalized optical power and the temperature fluctuation ΔT around $T_0 = 284$ mK. These simulations are performed at the detuning represented by the red dot in a) and b).

fitting parameters. The best results could be obtained with $\alpha_{abs} = 0.35$ and Γ being 1 Hz, 1.5 Hz and 5 Hz respectively for the input powers 3.4 pW, 6.8 pW and 68 pW, pointing towards an increase in the intrinsic damping rate with laser power. Such nonlinear damping has already been reported in the context of superfluid helium films [71], as well as silicon optomechanical crystals [22]. In addition to the strong dynamical back action, induced by the photo thermal effect, we observe a static photothermal effect in the simulations as well. As explained in the main text, this static effect is caused by the rise of the mean temperature of the superfluid film. In sub-figure e) of the figures 13, 14 and 15 it is shown that the mean temperature rises by about 0.2 mK, 0.37 mK and 3.6 mK respectively for the input powers 3.4 pW, 6.8 pW and 68 pW. This increase in temperature causes the superfluid film to thicken, shifting the optical mode. For the input power of 68 pW the optical mode is shifted by 19.6 MHz, corresponding to an optical tunability of 288 GHz/ μ W, as shown in Fig. 15(b). This DC thickening of the film is also apparent in Fig. 15(c), which shows the superfluid film oscillations around a new, thicker equilibrium position.

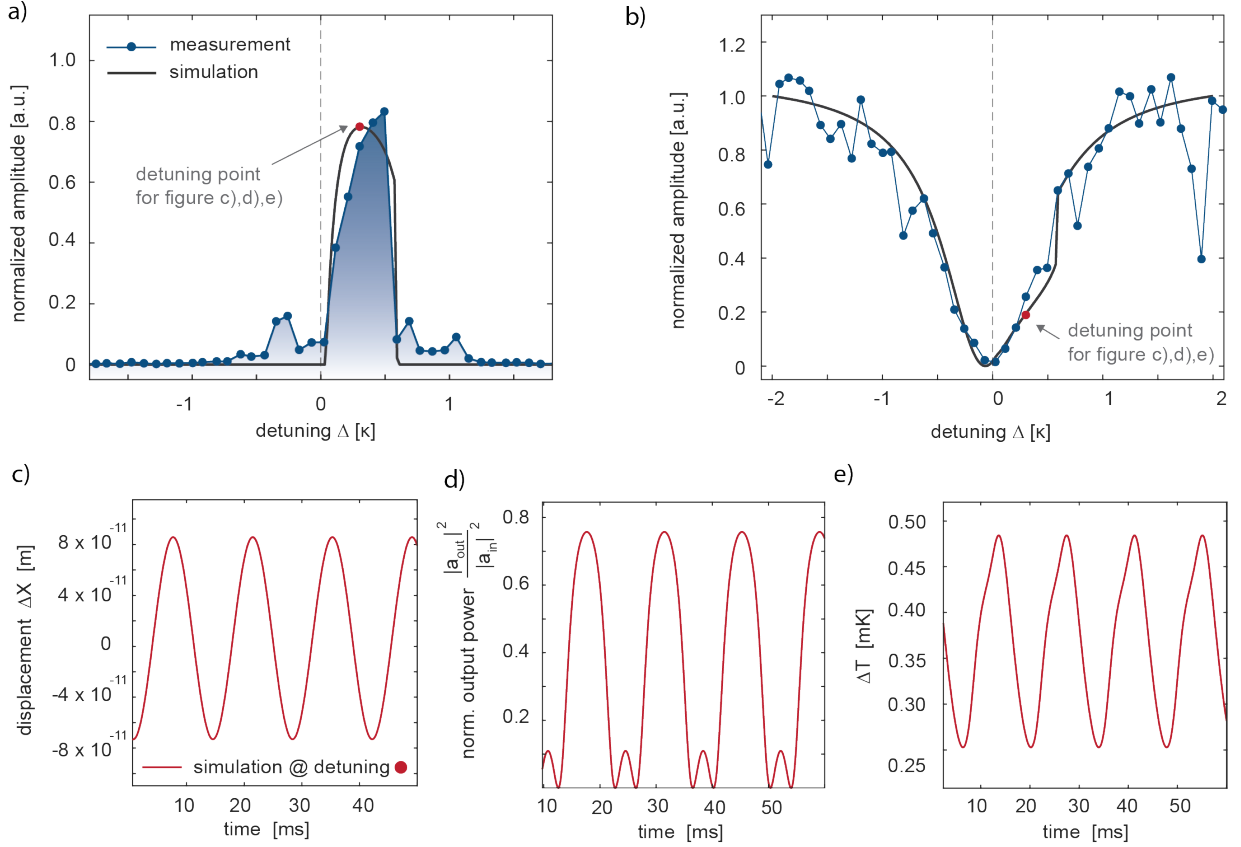


FIG. 14. Numerical simulation for 6.8 pW input power. a) Mechanical mode ($\Omega/2\pi i = 72$ Hz) amplitude as a function of cavity detuning, where the blue dots represent the normalized measured mode peak of the power spectrum and the black line the numerical simulations. b) Transmitted optical power from of the whispering gallery mode depending on the detuning, obtained by plotting the experimentally measured normalized spectral density peak value of the calibration peak at 180 Hz (blue dots) and the local oscillators (80 MHz) normalized spectral density peak value in the numerical simulations (black line). The numerical simulations in c), d) and e) show the time dependency in the steady-state regime of respectively the displacement ΔX , the cavity transmitted normalized optical power and the temperature fluctuation ΔT around $T_0 = 284$ mK. These simulations are performed at the detuning represented by the red dot in a) and b).

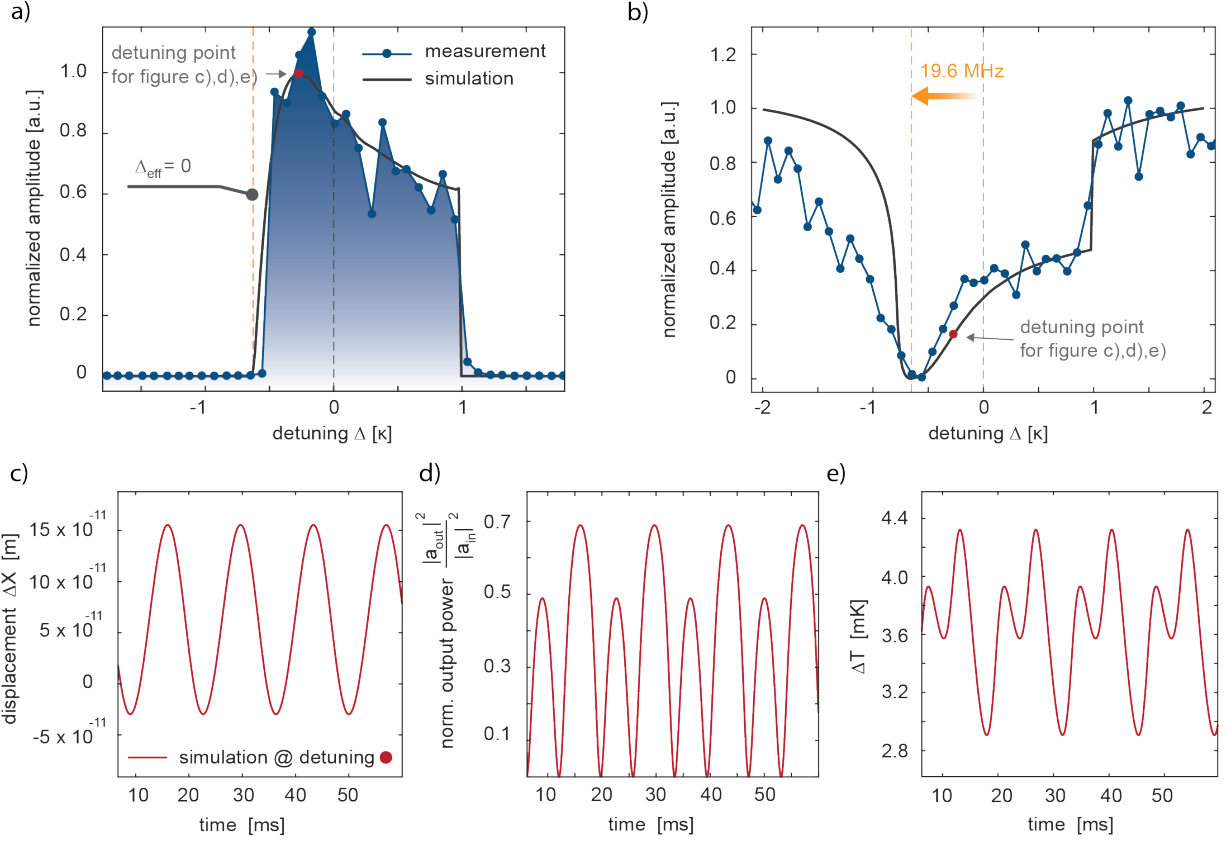


FIG. 15. **Numerical simulation for 68 pW input power.** a) shows the mechanical mode ($\Omega/2\pi i = 72$ Hz) amplitude depending on the cavity detuning, where the blue dots represent the normalized measured mode peak of the power spectrum and the black line the numerical simulations. b) Normalized optical transmission of the whispering gallery mode resonator as a function of detuning, obtained by plotting the experimentally measured normalized spectral density peak value of the calibration peak at 180 Hz (blue dots) and the local oscillators (80 MHz) normalized spectral density peak value in the numerical simulations (black line). At this high power, the D fountain pressure force causes the superfluid film to thicken, which leads to an optical resonance shift of 19.6 MHz. The numerical simulations in c), d) and e) show the time dependency in the steady state regime of respectively the displacement Δx , the cavity transmitted normalized optical power and the temperature fluctuation ΔT around $T_0 = 284$ mK. These simulations are performed at the detuning represented by the red dot in a) and b).

Parameter	Symbol	Value	Unit	Source
WGM intrinsic energy decay rate	$\kappa_i/2\pi$	15	MHz	measurement
WGM extrinsic energy decay rate	$\kappa_{\text{ex}}/2\pi$	15	MHz	measurement
Third sound mode frequency	$\Omega_M/2\pi$	72 86	Hz	measurement FEM
Third sound mode effective mass	m_{eff}	5.1×10^{-3}	kg	FEM
Third sound mode decay rate	Γ	$2\pi \times 1$	Hz	measurement
Optomechanical coupling strength	$G/2\pi$	0.2 ± 0.01	GHz/nm	FEM
Single photon optomechanical coupling rate	$g_0/2\pi$	0.7	Hz	FEM
Microsphere radius	R	49.5	μm	SEM
Mean superfluid film thickness	d_0	24	nm	measurement
Superfluid ^4He density	ρ_{He}	145	kg/m^3	[60]
First sound speed in superfluid helium	$c_{1\text{He}}$	236	m/s	[72]
superfluid helium mass (covering the total microsphere+stem)	m_{He}	2.65×10^{-12}	kg	FEM
Silica density	ρ_{SiO_2}	2200	kg/m^3	[73]
Silica thermal conductivity (@284 mK)	κ_{SiO_2}	1.6×10^{-3}	$\text{W}/\text{m}/\text{K}$	[74]
Silica specific heat capacity (@284 mK)	c_{SiO_2}	3.4×10^{-4}	$\text{J kg}^{-1} \text{ K}^{-1}$	[34]
Thermal conductance (@284mK)	$G_{\text{th-sub}}$	4.1×10^{-9}	W/K	FEM
Silica microsphere area (incl. stem)	\mathcal{A}	7.7×10^{-7}	m^2	SEM
Silica microsphere mass (incl. stem)	m_{sub}	4.9×10^{-8}	kg	FEM
Longitudinal sound velocity of silica	$c_{l\text{SiO}_2}$	5968	m/s	[75]
Transverse sound velocity of silica	$c_{t\text{SiO}_2}$	3764	m/s	[75]
Thermal response time	τ_{th}	5.7	ms	FEM
He II entropy per unit mass (@284 mK)	S	0.16	$\text{J}/\text{kg}/\text{K}$	[60]
fraction of κ_i dissipated as heat	α_{abs}	0.35	-	fit
Operating temperature	T	284	mK	measurement

TABLE III. Physical parameters used in the simulation. FEM:Finite Element modelling. SEM: Scanning electron microscope.

D.

Lasing thresholds for various systems

We benchmark our phonon lasing threshold against existing literature in Fig. 5 of the main text. We condensed the amount of systems shown in Fig. 5 to 14 different experiments, which are representative for the majority of phonon lasing systems and driving mechanisms (radiation pressure, electrostriction, photothermal and electrothermal interactions). All literature references that have been used for Fig. 5 are listed in Table IV.

E.

Thermodynamic efficiency

The thermodynamic efficiency is estimated by multiplying the stored mechanical power with the mechanical damping rate, yielding an acoustic power loss P_{mech} , which must be exactly compensated by the optical drive to maintain constant amplitude self-sustained oscillations.

$$P_{\text{mech}} = \frac{1}{2} m_{\text{eff}} \Omega^2 x^2 \Gamma \quad (\text{E1})$$

Using the values from table III and a displacement amplitude of $x = 6 \times 10^{-11}$ (obtained from Fig. 13), we get $P_{\text{mech}} = 1.2 \times 10^{-17}$ W; while the dissipated optical power is given by $P_{\text{abs}} = P \times \alpha_{\text{abs}} = 3.4 \text{ pW} \times 0.35 = 1.2 \text{ pW}$. This results in a thermodynamic efficiency (rate of conversion of heat into mechanical work) of $\eta = P_{\text{mech}}/P_{\text{abs}} = 1 \times 10^{-5}$.

As a comparison we calculate the thermodynamic efficiency for the carbon nanotube electrothermal system with the closest lasing threshold ($\sim 5 \text{ pW}$) [24]. The mechanical power produced to sustain phonon-lasing is:

$$P_{\text{mech}}^{\text{nano}} = \frac{1}{2} m_{\text{eff}}^{\text{nano}} \Omega_{\text{nano}}^2 x_{\text{nano}}^2 \Gamma_{\text{nano}} = 4.3 \times 10^{-19} \text{ W}, \quad (\text{E2})$$

with the effective mass $m_{\text{eff}}^{\text{nano}} = 2.7 \times 10^{-21}$ kg, the mechanical frequency $\Omega_{\text{nano}}/(2\pi) = 90 \text{ MHz}$, the displacement $x_{\text{nano}} = 4 \text{ nm}$ and the mechanical decay rate $\Gamma_{\text{nano}}/(2\pi) = 10 \text{ Hz}$ [24]. The electrical power dissipated as heat required for the production of $P_{\text{mech}}^{\text{nano}}$ is approximately $P_{\text{elec}} = 5 \text{ pW}$. This results in a thermodynamic efficiency for the nanotubes $\eta_{\text{nano}} = P_{\text{mech}}^{\text{nano}}/P_{\text{elec}} = 0.86 \times 10^{-7}$. This comparison indicates our system is $\sim 10^2$ times more thermodynamically efficient than the nanotube system with the lowest reported lasing threshold, aside from ours.

F.

Single photon detection

The fountain pressure between a region of the film at temperature T , and a bath at temperature T_0 corresponds to

$$P_{\text{fp}} = \rho \int_{T_0}^T S(T') dT' \quad (\text{F1})$$

For a small difference in temperature, the fountain pressure is given by [33, 34]:

$$P_{\text{fp}} = \rho S \Delta T \quad (\text{F2})$$

At low temperatures, the specific heat of superfluid helium is several orders of magnitude larger than that of the underlying optical resonator material (e.g. silicon, silica) [76]. For instance, at 250 mK, $c_{\text{He}} \simeq 1000 c_{\text{SiO}_2}$. Therefore for miniature optical resonators, where the thickness of the superfluid film is no longer negligible compared to that of the resonator (consider e.g. a 30 nm thick superfluid film on either side of a 200 nm thick resonator), the entire thermal mass of the superfluid-covered resonator is dominated by the superfluid film. The temperature increase for a deposited energy Q corresponding to one absorbed photon is therefore given by:

$$\Delta T = \frac{Q}{m c_{\text{He}}} = \frac{\hbar \omega}{m c_{\text{He}}}, \quad (\text{F3})$$

where m is the mass of the superfluid film, and c_{He} superfluid helium's specific heat capacity. Since the superfluid helium entropy takes the form [60]:

$$S = \int \frac{c_{\text{He}}}{T} dT, \quad (\text{F4})$$

for c_{He} of the form αT^3 ,

$$S = \int \frac{\alpha T^3}{T} dT = \int \alpha T^2 dT = \frac{\alpha T^3}{3} \simeq \frac{c_{\text{He}}}{3} \quad (\text{F5})$$

#	mechanical frequency	effective mass	lasing threshold	driving mechanism	Source
1	90 MHz	2.7×10^{-21} kg	~ 5 pW	electrothermal	C. Urgell, et al, <i>Nature Physics</i> vol. 16 , pp.32-37 (2020)
2	230 MHz	2.2×10^{-20} kg	~ 10 pW	electrothermal	Y. Wen, et al, <i>Nature Physics</i> vol. 16 , pp.75-82 (2020)
3	3.5 MHz	2×10^{-16} kg	500 nW	photothermal	R.A. Barton, et al, <i>Nano Letters</i> vol. 12 , 9 , pp. 4681-4686 (2012)
4	3 MHz	2.1×10^{-16} kg	660 nW	photothermal	R.De Alba, et al, <i>Nano Letters</i> vol. 17 , 7 , pp.3995-4002 (2017)
5	180 kHz	1.6×10^{-12} kg	30 μ W	photothermal	D. Wolf, et al, <i>Optics Express</i> vol. 21 , 6 , pp. 7258-7275 (2013)
6	8 kHz	2.3×10^{-12} kg	26 μ W	photothermal	C. Metzger, et al, <i>Physical Review Letters</i> vol. 101 , 133903 (2008)
7	7.3 MHz	1.2×10^{-14} kg	1.8 μ W	photothermal/radiation pressure	X. He, et al, <i>Nature Physics</i> vol. 16 , pp.417-421 (2020)
8	314 MHz	5.3×10^{-14} kg	~50 μ W	photothermal/radiation pressure	P.E. Allain, et al, <i>Physical Review Letters</i> vol. 126 , 243901 (2021)
9	3 GHz	2.7×10^{-16} kg	2.5 mW	radiation pressure	L. Mercade, et al, <i>Nanophotonics</i> vol. 9 (11), pp.3535-3544 (2020)
10	3 GHz	1.0×10^{-15} kg	40 μ W	photoelastic	I. Ghorbel, et al, <i>APL Photonics</i> vol.4, pp.116103 (2019)
11	2 MHz	7.6×10^{-15} kg	60 μ W	radiation pressure	H. Jayakumar, et al, <i>Phys. Rev. Applied</i> vol. 16 , 014063 (2021)
12	23 MHz	5.0×10^{-11} kg	7 μ W	radiation pressure	I. Grudinin, et al, <i>Physical Review Letters</i> vol. 104 , 083901 (2010)
13	1.2 GHz	5.7×10^{-15} kg	3 μ W	radiation pressure	W.C. Jiang, et al, <i>Optics Express</i> vol. 20 ,14, pp. 15991-15996 (2012)
14	8 MHz	1.5×10^{-13} kg	270 nW	radiation pressure	Q. Lin, et al, <i>Physical Review Letters</i> vol. 103 , 103601 (2009)
15	3.7 GHz	3.1×10^{-16} kg	~ 500 nW	radiation pressure/electrostriction	A. Krause et al, <i>Physical Review Letters</i> vol. 115 , 233601 (2015)
16	3.6 GHz	$\sim 0.3 \times 10^{-15}$ kg	7 nW	radiation pressure/electrostriction	S. Meenahan et al, <i>Phys. Rev. A</i> vol. 90 , 011803 (2014)

TABLE IV. Sources used to compare the lasing thresholds for various systems in Fig.5.

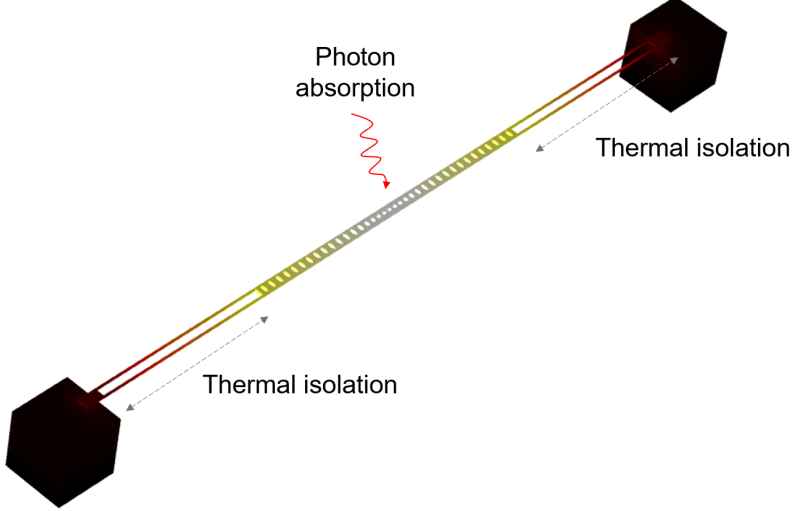


FIG. 16. Silicon 1D photonic crystal architecture. Long tethers provide thermal isolation from the substrate.

(Which is indeed what is measured in practice, see ref. [60]). Using this, we can re-express Eqs. (F2) and (F3) as:

$$P_{fp} = \frac{\rho S(T) \hbar \omega}{\rho V c_{He}(T)} \quad (F6)$$

and obtain a simple, temperature-independent expression for the induced fountain pressure resulting from the absorption of a photon of energy $\hbar \omega$:

$$P_{fp} \simeq \frac{\hbar \omega}{3 V_{He}} \quad (F7)$$

The goal is therefore to minimize the volume of superfluid covering the resonator, which is attained by reducing the resonator surface area. The above calculation is valid in the regime where:

- The thermal response time of the resonator is slower than that of the superfluid film (which is on the order of a few microseconds at the temperatures considered here), allowing the thermal energy to be transferred to the superfluid film before it is lost to the environment through the resonator's own thermal anchoring.
- The thermal Kapitza conductance at the resonator/superfluid interface is well in excess of the thermal conductance between the helium film and its environment mediated through the vapor pressure. This allows heat to build up in the superfluid film before it is lost to the environment through evaporation. This criterion does not depend strongly on the choice of resonator material³, and is valid for temperatures below ~ 300 mK.

An example architecture satisfying the above conditions is shown in Fig. 16. It consists of a suspended 1D silicon optical crystal cavity, of the kind used in Ref. [2]. Long and narrow tethers provide sufficient thermal isolation for the heat resulting from optical absorption to be predominantly communicated to the superfluid film. Such a resonator has a optomechanical coupling rate simulated through FEM of $G/2\pi = \sim 5$ GHz/nm [40], (meaning that a 1 nm change in thickness of the superfluid film shifts the optical resonance frequency by 5 GHz). Using Eq. F7, we estimate a thickening of the film on the order of 1 nm is achievable per absorbed photon, leading to an optical shift well in excess of the optical resonator linewidth κ [2].

³ Since the acoustic impedance mismatch between superfluid helium and most solids commonly used for optical resonator fab-

rication (Silica, Silicon, Gallium Arsenide...) is of comparable magnitude.

F.

Comparison to radiation pressure per photon

We compare the magnitude of the fountain pressure induced by a photon absorption event (Eq. F7) to the radiation pressure exerted by an intracavity photon. The radiation pressure due to a single photon acting on an element of the superfluid film—which arises due to the change in electromagnetic energy density due to the presence of the helium—is given by:

$$P_{\text{rad}} = \frac{1}{2} \varepsilon_0 (\varepsilon_{\text{sf}} - 1) E^2, \quad (\text{F8})$$

where the electric field is normalized such that:

$$\frac{1}{2} \iiint \varepsilon_0 \varepsilon_r(\vec{r}) E^2 dV = \hbar\omega. \quad (\text{F9})$$

Making the (strongly) simplifying assumption that the field be essentially localized within the optical resonator (of permittivity ε_r) and of constant magnitude over the mode volume V_{mode} , leads to $E^2 \sim \hbar\omega / (1/2 \varepsilon_0 \varepsilon_r V_{\text{mode}})$. Combined with Eq. (F8), this provides an order of magnitude estimate of achievable the radiation pressure per photon acting on the superfluid film:

$$P_{\text{rp}} \simeq \frac{\varepsilon_{\text{sf}} - 1}{\varepsilon_r} \frac{\hbar\omega}{V_{\text{mode}}} \quad (\text{F10})$$

Compared to Eq. (F7), we note the presence of the prefactor ($\frac{\varepsilon_{\text{sf}} - 1}{\varepsilon_r} = 5 \times 10^{-3}$ for a silicon resonator), and the fact that the superfluid volume has been replaced by the (larger) optical mode volume. Combined, these two effects lead to an approximate 3 orders of magnitude reduction compared to the fountain pressure, see Eq. (F7).

G.

Comparison with thermo-elastic stress in a crystal

The thermal stress σ_{th} arising from a temperature increase ΔT in an isotropic solid of bulk modulus K and thermal expansion coefficient $\alpha = \frac{1}{V} \left(\frac{\partial V}{\partial T} \right)$ is given by:

$$\alpha \Delta T = \frac{\sigma_{\text{th}}}{K}, \quad (\text{G1})$$

where for one absorbed photon, ΔT is given by:

$$\Delta T = \frac{\hbar\omega}{\rho V c} \quad (\text{G2})$$

This yields a thermal stress per photon of

$$\sigma_{\text{th}} = \frac{\hbar\omega \alpha K}{\rho V c} \quad (\text{G3})$$

This can be re-expressed in simpler form as:

$$\sigma_{\text{th}} = \gamma \frac{\hbar\omega}{V}, \quad (\text{G4})$$

where we have introduced the dimensionless Grüneisen parameter $\gamma = \frac{\alpha K}{\rho c}$. For silicon at low temperatures, this takes a value of approximately $\gamma \simeq 0.2$ [77], resulting in a thermal stress very close to the superfluid fountain pressure (Eq. (F7)). It is thus primarily the compliance of the fluid interface, combined with the engineered ability to collect the thermal energy and operate near the optimal regime $\Omega\tau \sim 1$ which is responsible for the ultralow threshold observed here, and not a fundamentally stronger nature of the fountain pressure force in superfluid helium, making these results broadly applicable to photothermally- and electrothermally-driven systems.